Interior Structure Modelling of Low Mass Exoplanets with Constraints

Modellierung der Innenstruktur von Exoplaneten geringer Masse mit Einschränkungen

Master thesis | Masterarbeit

For the acquirement of the scientific degree
Master of Science
in the discipline of Astrophysics

Verfasser:	Aleeda Charly
Studiengang:	Deutsches Zentrum für Luft und Raumfahrt, Berlin
Matrikelnummer:	816508
Erstgutachter:	Dr. Nicola Tosi
Zweitgutachter:	Prof Dr. Stephan Geier

Statement of Originality

This thesis is the result of my own work conducted at Deutsches Zentrum für Luft- und Raumfahrt (DLR) Berlin, under the supervision of Dr. Nicola Tosi. The research presented herein is original and has not been submitted, in whole or in part, for any degree or professional qualification at this or any other institution.

Where the work of others has been utilized, it has been fully acknowledged and appropriately referenced. Any collaborative work or contributions by others to this research has been explicitly stated and cited in the relevant sections of this thesis.

Aleeda Charly
19 February 2025

Acknowledgements

I would like to express my deepest gratitude to my supervisor, Dr. Nicola Tosi, for his unwavering guidance, encouragement, and insightful feedback throughout the course of this research. His expertise and support have been invaluable to this thesis.

I am immensely grateful to my friend, Dr. Philipp Baumeister, for his patience, mentorship, and assistance in helping me understand the codes critical to my work. Without his guidance, much of this research would not have been possible.

I would also like to thank Prof. Dr. Doris Breuer, Head of the Department of Planetary Physics, for giving me the opportunity to undertake this research and for her encouragement and support.

Additionally, I extend my thanks to my colleagues and friends at Planetary Physics research group at DLR for fostering and inspiring and collaborative work environment. Their discussions, ideas, and camaraderie have greatly enriched this journey.

Zusammenfassung

Das Verständnis der inneren Struktur von massearmen Exoplaneten ist eine grundlegende Herausforderung für die Planetenforschung, insbesondere angesichts der inhärenten Entartungen bei der Modellierung ihrer inneren Zusammensetzung. Diese Arbeit befasst sich mit dieser Herausforderung, indem sie sich auf die Wasser- und Gasschichten konzentriert, da diese flüchtigen Stoffe die Planetenradien durch die Veränderung von Dichte- und Druckgradienten erheblich beeinflussen, was erhebliche Unsicherheiten in bestehende Modelle einbringt. Das Hauptziel besteht darin, diese Entartung zu verringern und klarere Erkenntnisse über die Zusammensetzung und die strukturellen Merkmale dieser Planeten zu gewinnen, die für die Interpretation von Beobachtungsdaten und die Bewertung der Bewohnbarkeit entscheidend sind.

Um dieses Problem anzugehen, verwende ich ein auf Mixture Density Networks (MDNs) basierendes maschinelles Lernmodell namens ExoMDN, um die inneren Strukturen von massearmen Exoplaneten zu untersuchen. ExoMDN wurde auf einer Datenbank mit 5,6 Millionen vorberechneten synthetischen Innenstrukturen trainiert und ermöglicht schnelle probabilistische Schlüsse auf das Innere von Planeten in weniger als einer Sekunde. Im Gegensatz zu herkömmlichen Methoden, die eine umfangreiche Modellierung jedes Planeten erfordern und deren Berechnung mehrere Tage dauern kann, ist ExoMDN aufgrund seiner Effizienz ideal für groß angelegte Studien. Dieser Vorteil ermöglicht es mir, das Innere von Planeten umfassend zu erforschen, was mit herkömmlichen Methoden sehr rechenintensiv wäre.

Diese Arbeit trägt zu einem tieferen Verständnis der Beziehung zwischen der Zusammensetzung von Planeten, dem Gehalt an flüchtigen Bestandteilen und beobachtbaren Eigenschaften wie Masse und Radius bei. Die Ergebnisse haben erhebliche Auswirkungen auf künftige Beobachtungsmissionen wie PLATO, deren Ziel es ist, Exoplaneten mit hoher Präzision zu charakterisieren und ihre potenzielle Bewohnbarkeit zu erforschen. Darüber hinaus unterstreicht diese Arbeit, wie wichtig es ist, Einschränkungen durch Planetenentstehung und atmosphärische Entweichungsmodelle zu integrieren, um die Genauigkeit der Vorhersagen über die innere Struktur zu verbessern.

Abstract

Understanding the interior structure of low-mass exoplanets is a fundamental challenge in planetary science, particularly given the inherent degeneracies in the modeling of their internal compositions. This thesis addresses this challenge by focusing on the water and gas layers, as these volatiles significantly influence planetary radii by altering density and pressure gradients, introducing substantial uncertainty in existing models. The primary objective is to reduce this degeneracy and provide clearer insights into the compositional and structural characteristics of these planets, which are crucial for interpreting observational data and assessing habitability.

To tackle this issue, I employ a machine-learning model based on Mixture Density Networks (MDNs) called ExoMDN to study the interior structures of low-mass exoplanets. Trained on a database of 5.6 million precomputed synthetic interior structures, ExoMDN enables rapid probabilistic inference of planetary interiors in under a second. Unlike traditional methods, which require extensive modeling for each planet and can take several days to compute, ExoMDN's efficiency makes it ideal for large-scale studies. This advantage allows me to comprehensively explore planetary interiors that would otherwise be computationally expensive with conventional approaches.

This thesis contributes to the field by providing a deeper understanding of the relationship between planetary composition, volatile content, and observable properties such as mass and radius. The results have significant implications for future observational missions like PLATO, which aim to characterize exoplanets with high precision and explore their potential habitability. Furthermore, this work underscores the importance of integrating constraints from planet formation and atmospheric escape models to enhance the accuracy of interior structure predictions.

Contents

Introduction

The idea of innumerable worlds revolving around stars existed from the very early ancient Greek civilization. We are the first generation in the history of mankind to know that the hypothesis of these worlds is actually true. The discovery of the first exoplanet around the solar-type star 51 Peg by radial velocity method (Mayor & Queloz 1995) was not only striking for the astronomical community but kick-started the field of exoplanetary science along with the study of the formation and evolution of planets in different stellar systems. This planetary system was unlike anything we knew of from our own solar system. The planet 51 Peg b had a period of 4.23 days and a minimum mass of 0.5 M_J(Jupiter Mass), making it a so-called Hot Jupiter, orbiting very close to its parent star. After this discovery, we now have a plethora of different types of planets around different types of stars in our galaxy.

Data from the Kepler missions (Borucki et al. 2010) have revealed a new set of planets called "super-Earths" and "sub-Neptunes", for which we have no analogs in our solar system. Super-Earths are planets with a radius of $1 - 1.75\,R_\oplus$, which are typically rocky, and sub-Neptunes are planets with a radius of $1.75 - 3.5\,R_\oplus$, presumably with substantial amount of hydrogen-helium atmospheres (Fulton et al. 2017). Both super-Earths and sub-Neptunes fall into the category of low-mass exoplanets, typically having masses less than $30M_\oplus$ (Jontof-Hutter 2019). The discovery of such planets with unusual features questioned the current theories of how planetary systems could form and how they have evolved. We have now confirmed over 5600 (NASA Exoplanet Archive, 2024) exoplanets through various detection methods. Planets within the habitable zone (HZ)—defined as the region around a star where the temperature range may allow liquid water to exist on the planet's surface (Huang 1959; Dole 1964; Kasting et al. 1993)—have garnered significant attention. Studying these diverse planets not only provides insight into these distant worlds, but also enhances the understanding of our own solar system. By examining their formation, evolution and interior structures, we can better assess their potential habitability and lay the groundwork for future searches of life beyond the Earth.

1.1 Scope of the Thesis

My work aims at improving the characterization of exoplanetary interiors by addressing the degeneracy that arises from the observable mass and radius of low mass exoplanets. This degeneracy refers to the fact that multiple interior compositions can produce the same observed mass and radius (Rogers & Seager 2010; Lopez & Fortney 2014; Dorn et al. 2015, 2016; Lozovsky et al. 2018), making it challenging to determine the precise internal structure of these planets.

The thesis work is focused on four key areas:

1. **Parameter Constraints**: For a given planetary mass and radius, I explored the range of possible interior configurations of exoplanets up to 5 Earth masses, consisting of four distinct layers (metallic core, silicate mantle, water layer, and H/He atmosphere). In particular, I studied the influence on the interior predictions of varying the mass fractions of the water and gas (H/He atmosphere) layers. These two components are crucial because, due to their relatively low density, they affect strongly the determination of the planetary radius. I discuss ways to reduce the overall degeneracy of the interior by restricting the range of variability of the two parameters.

2. **Utilization of Population Synthesis and Atmosphere Loss Models**: To strengthen the physical basis of the assumed constraints on water and gas mass fractions, I discussed results from models of planet population synthesis and atmosphere loss, respectively. This will lead to a better understanding of the likely interior composition in relation to planet formation theories and atmospheric evolution.

3. **Comparative Analysis of Terrestrial Analogue Interiors**: I carried out a comparative study of different sizes and interior structures, focusing on planets with Earth -like, Mercury-like, and Moon-like compositions. This analysis will highlight how varying compositions and densities among planets will result in diverse interior structures, even among planets with similar masses and radii.

4. **Impact of Observational Uncertainties**: Recognizing the inherent uncertainties in observations is a crucial aspect of characterizing the interior structure. I investigated how these uncertainties impact the inference of interior structures.

1.2 Structure of the Thesis

The structure of the thesis is as follows: Chapter 2 provides an discussion of planet detection methods, the observed populations of planets, and their characteristics, and introduces the fundamentals of interior structure modeling. Chapter 3 details the methodologies employed in interior modeling of low-mass exoplanets, including a new approach for constraining planetary interior structures. Chapter 4 presents the results of the study along with an in-depth analysis of the findings. Chapter 5 discusses the findings within the context of existing research and theories. Finally, Chapter 6 summarizes the thesis and provides an outlook on potential future research directions.

Low Mass Exoplanets and Modelling of their Interior Structure

Low mass exoplanets exhibit extreme diversity in mass, radius and therefore their bulk densities (Jontof-Hutter et al. 2016). As measurement techniques for these parameters become increasingly precise, characterizing their interior structure becomes crucial, providing insights into their formation history, evolution and potential habitability. Nevertheless, with precise measurements, the interior structure modelling remains challenging due to degeneracies, as similar mass and radius values can correspond to different interior compositions.

This chapter begins by discussing the detection methods commonly used for identifying exoplanets, followed by an introduction to low-mass exoplanets, including their unique properties and significance. Finally, it explores strategies for reducing degeneracies in interior structure modeling, which are crucial for accurately characterizing these planets.

2.1 Detection Methods

Over the past few decades, significant progress has been made in detections methods for finding and characterizing various types of exoplanets around different types of stars. Mass measurements, combined with radius determinations, allow us to characterize these planets by their bulk densities (Sohl et al. 2012; Laughlin 2018). The first exoplanetary discovery was achieved by measuring periodic radial velocity variation in stellar spectra using ground-based spectrographs (Mayor & Queloz 1995). Since then, we have leveraged the properties of the stars and planets around them to discover new worlds. The primary methods are of transit photometry and radial velocity measurements. Other methods, such as microlensing (Einstein 1936; Bond et al. 2004; Beichman & Deming 2018; Udalski 2018; Han et al. 2024), direct imaging (Lagrange et al. 2010; Mennesson et al. 2016; Pueyo et al. 2017), and astrometry (Sozzetti 2010), pulsar timing (Kramer 2018), pulsation timing variation (Hermes 2018), orbital brightness modulation (Limbach et al. 2022), eclipse timing variations (Schwarz et al. 2015) and transit timing variation (Agol & Fabrycky 2018) have also been successful but yield significantly lower detection rates. The cumulative number of planet detections with different methods are illustrated in Figure 2.1. In this section, we will focus on transit surveys and radial velocity method for detecting exoplanets.

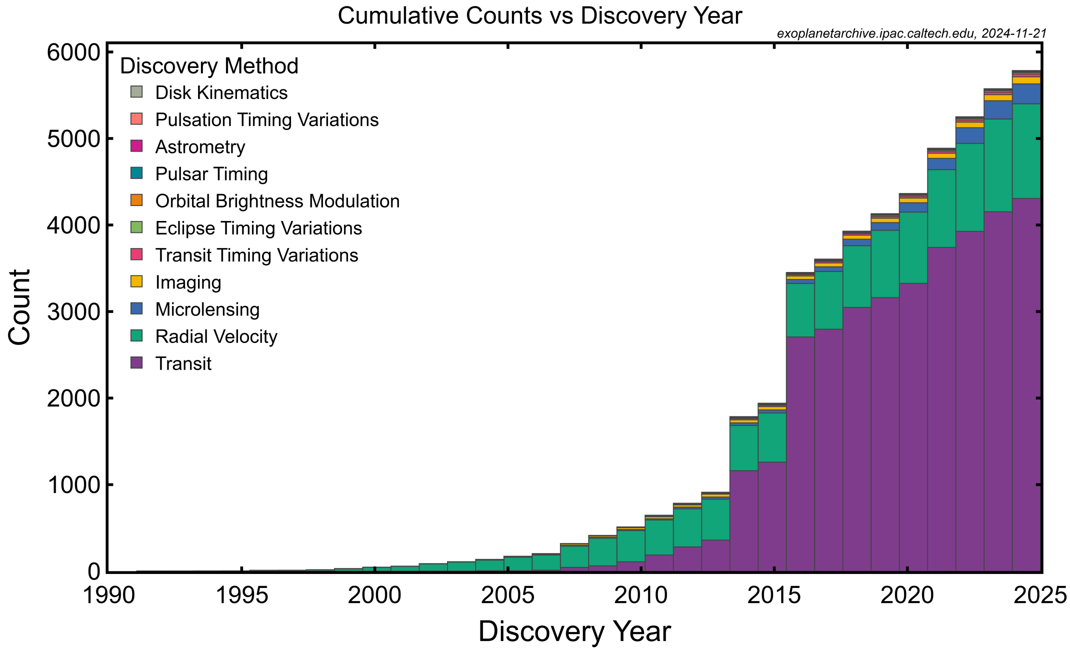

Figure 2.1: Cumulative number of planet detections per year since 1992 from different methods. [Image credits: NASA Exoplanet Archive].

2.1.1 Radial Velocity Method

The radial velocity method laid the foundation for the exoplanet studies through the discovery of the first exoplanet around a Sun-like star (Mayor & Queloz 1995). To date, almost 1000 exoplanets have been detected by this method, which supports transit searches by providing planetary masses, essential for characterizing the planets through theirs bulk density. The basic principle behind the radial velocity method involves measuring the line-of-sight (radial) velocity component of a star as it moves around the center of mass of the planetary system. This phenomenon, known as Doppler shift, occurs when the wavelength of the star's spectral lines shifts due to it's motion and is shown in Figure 2.2. The semi-amplitude (K) of the star's radial velocity can be computed as follows (Wright 2018):

$$K \approx \left(\frac{2\pi G}{PM_\star^2}\right)^{\frac{1}{3}} \frac{M_{\text{planet}} \sin i}{\sqrt{1-e^2}} \tag{2.1}$$

where e is the orbital eccentricity, i is the inclination of the orbit relative to the sky plane, M_{planet} is the mass of the planet, $M_\star$ is the mass of the host star, and P is the orbital period. The ability of detect exoplanets with precise radial velocity measurements thus depends on planet's mass, inclination and orbital period (it also depends on eccentricity but less pronounced for planets with low eccentricities). Because the inclination angle (i) is generally unknown, the true mass of the planet could be larger, depending on the inclination. Therefore, the measured value is often called the **minimum mass** of the planet.

A Jupiter mass planet closer to our Sun-like star would induce a stellar reflex motion with an amplitude of a few hundreds of $\mathrm{m\,s^{-1}}$. We see here why the first strong exoplanet detections (Latham et al. 1989; Mayor & Queloz 1995) were of Jupiter-like planet in short-period orbit.

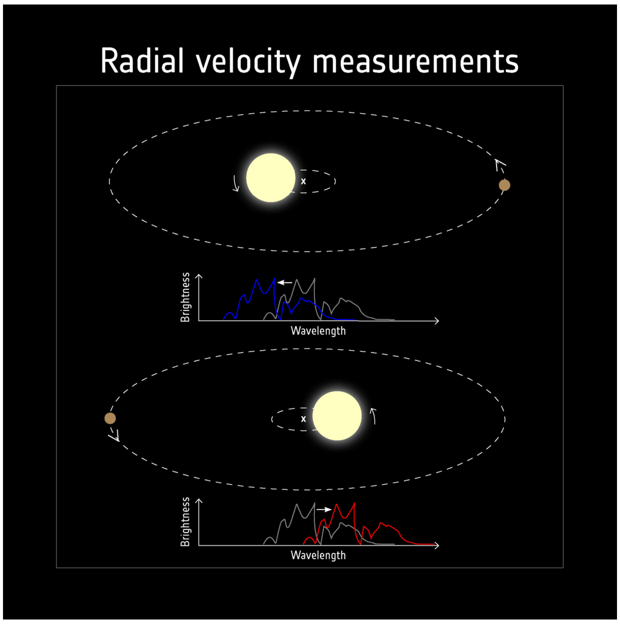

Figure 2.2: The gravitational pull of an orbiting planet causes velocity variations in the host star, which induce a Doppler shift in the star's spectrum. These shifts can be used to infer the planet's mass and orbital parameters [Image credits: ESA].

In contrast, an Earth-sized planet at 1AU would generate a much smaller reflex motion of just $10\ \mathrm{cm\,s^{-1}}$ (Hatzes 2016). If an Earth-sized planet were located at 0.05AU, the induced reflex motion would only increase to $\approx 1\ \mathrm{m\,s^{-1}}$. Detecting such small signals requires thus highly precise measurements. Instruments like the Near InfraRed Planet Searcher- NIRPS (Étienne Artigau et al. 2024), a near-infrared counterpart to the High Accuracy Radial velocity Planet Searcher (HARPS) (Unger et al. 2021) on the 3.6m telescope at La Silla Observatory, are designed for such precision. Additionally, the Echelle SPectrograph for Rocky Exoplanet and Stable Spectroscopic Observations (ESPRESSO) on the Very Large Telescope (VLT) is the first spectrograph specifically designed to achieve a precision of $20\ \mathrm{cm\,s^{-1}}$ (Pepe et al. 2010, 2014).

2.1.2 Transit Surveys

As of today, the transit method surpasses all other techniques in terms of number of exoplanet detections. The discovery of HD 209458 b (Henry et al. 2000; Charbonneau et al. 2000) marked the advent of exoplanets detection using this method. Space-based photometric missions such as Kepler (Borucki et al. 2010; Howell et al. 2014) and TESS (Ricker et al. 2014) have significantly contributed to this success by continuously monitoring hundreds of stars over periods ranging from weeks to years. An illustration of the transit method is shown in Figure 2.3. When a planet transits in front of its host star, the star's flux diminishes by a factor ΔF. Assuming negligible flux contribution from the planet and considering both star and planet as spherical bodies, ΔF is given by the ratio of the areas of planet and star, expressed as (Deeg & Alonso 2018):

$$\Delta F \approx \left(\frac{R_p}{R_s}\right)^2 = k^2 \tag{2.2}$$

where R_p is the radius of the planet, R_s is the radius of the star, and k is the radius ratio. For Sun-like stars, this ratio is usually at most 1%, but for stars with smaller radii, this ratio can be a few percent larger for Jupiter-like planets. The probability of detecting transiting planets

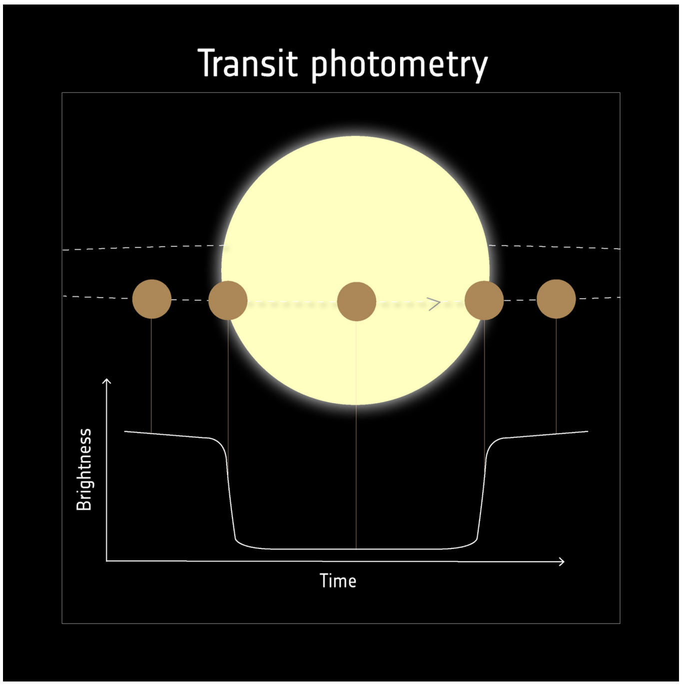

Figure 2.3: The transit method involves observing the dimming of a star's brightness when a planet transits in front of it. [Image credit: ESA]

depends on the planet's size, the star's size, and the distance between them. For a typical Hot Jupiter with a semi-major axis of 0.05 AU, this probability is of the order of 10%, but it drops to 0.5% for an Earth-sized planet at 1 AU from it's host star (Winn 2010). This low probability is a significant challenge in finding an Earth-like planet around Sun-like stars, as most planetary systems will not exhibit transits. Several transit surveys, including OGLE-III (Konacki et al. 2003), Kepler (Borucki et al. 2010), WASP (Smith et al. 2014), TESS (Ricker et al. 2014), NGTS (Wheatley et al. 2017) and CoRot (Deleuil et al. 2018), and have been successful in detecting planets. The upcoming ESA mission PLATO (PLanetary Transits and Oscillations of stars) (Rauer et al. 2014), is scheduled for launch in 2026 to the L2 point. PLATO is expected to operate for at least four years and is designed to detect Earth-like planets around Sun-like stars in their HZ.

2.2 The Diversity of Low-Mass Exoplanets

The Kepler mission (Borucki et al. 2010) has significantly expanded our knowledge of low-mass exoplanets whose masses ranging from 1-30$M_\oplus$. The interior structures of these exoplanets can be explained by various bulk compositions (Seager et al. 2007; Wang et al. 2022). This discovery has shifted the focus of exoplanetary composition studies toward terrestrial regimes. Our solar system showcases a wide range of planetary bulk compositions. Rocky planets inside the snow line are volatile-poor, while more massive, low-density planets beyond the snow line are rich in volatiles like hydrogen and helium (Raymond et al. 2014). There is an observed gap in both mass and radii that separates rocky planets from ice giants within our own solar system.

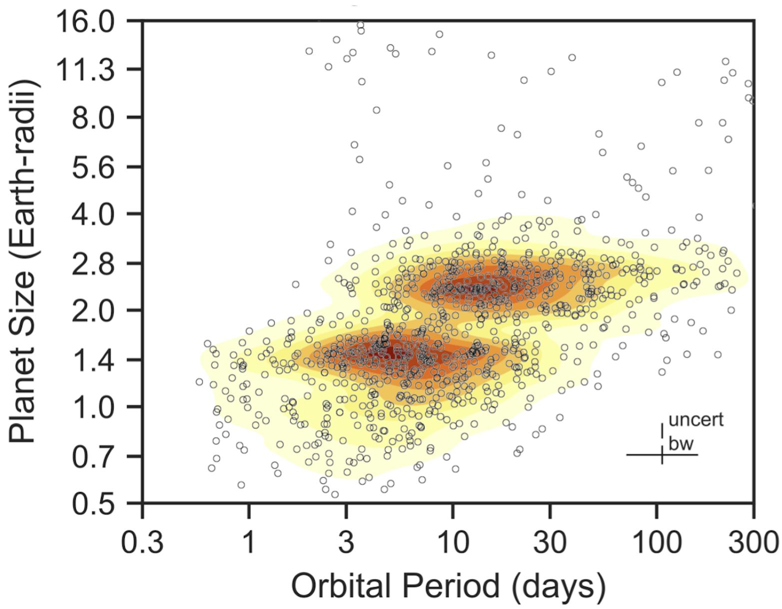

Figure 2.4: Detected planets from California-Kepler Survey (CKS) indicating populations of super-Earths and sub-Neptunes showing the bimodality in the radius-period diagram referred as "evaporation valley" or "radius valley" or "radius gap" (from (Petigura et al. 2022)).

The Kepler mission has shown that exoplanets with radii between $1R_\oplus$ and $4R_\oplus$ are very common, particularly among those with periods of less than 100 days (Mulders et al. 2015, 2018). The radius-period relation showed two peaks in the distribution of this close-in exoplanets at approximately $1.3R_\oplus$ and $2.4R_\oplus$ (Borucki et al. 2011) as shown in Figure 2.4. This bimodality in size hints at a separation due to composition, with planets smaller than $1.7R_\oplus$, as super-Earths, having a predominantly rocky composition, and less dense planets which retained a large amount of volatiles classified as sub-Neptunes (as shown in Figure 2.5). The addition of even a small amount of a gaseous envelope, due to its low density, leads to a disproportionate increase in planetary radius. This effect makes planets with radii in the 1.6–$1.8R_\oplus$ range rare among low-mass planets, as their sizes tend to shift either below this range (rocky planets) or above it (volatile-rich planets), even without considering atmospheric mass loss (Owen & Wu 2017). This observations hints to the possibility of various planet structure and continuum of bulk densities that bridges rocky and gaseous compositions. The intermediate densities of these planets suggest a significant amount of volatiles, though their exact nature is still not certain. There are two main theories to explain the existence of these two populations of exoplanets: the atmospheric dichotomy and the compositional dichotomy, which we describe below.

2.2.1 Atmospheric Dichotomy

The theory of atmospheric dichotomy suggests suggests that sub-Neptunes are planets with primordial H/He envelopes and super-Earth are those which lost their primordial envelopes.

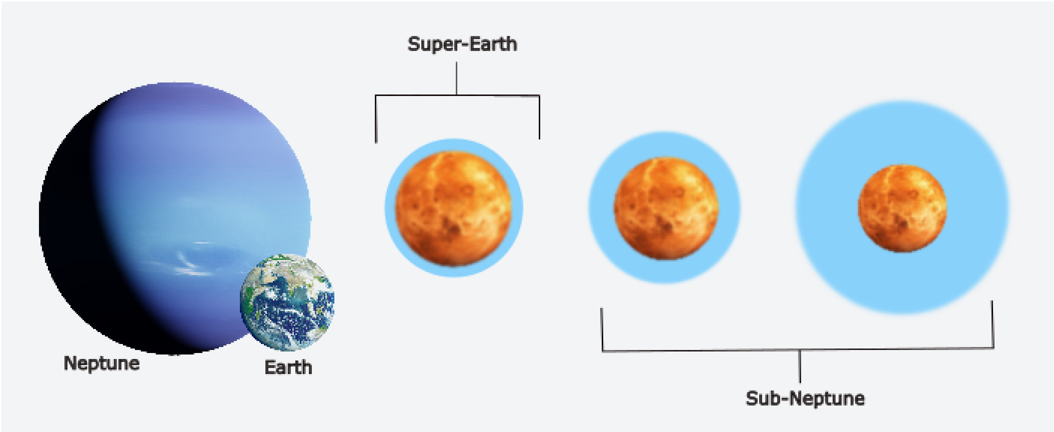

Figure 2.5: Super-Earths and Sub-Neptunes, highlighting their compositional differences. Super-Earths are predominantly rocky planets with minimal or no gaseous envelopes, while Sub-Neptunes typically possess a rocky core surrounded by a significant layer of volatiles, such as water, hydrogen, or helium (Mordasini et al. 2009; Owen & Wu 2017; Venturini et al. 2020). Another model proposes that some Sub-Neptunes could be water-rich, with a substantial fraction of their mass in the form of water or ices, depending on their formation and evolutionary pathways (Chakrabarty & Mulders 2024; Lozovsky & Vazan 2024; Burn et al. 2024).

There are different mass loss mechanisms that can cause low-mass planets to lose their primordial atmosphere. These include photo-evaporation caused by high stellar flux from young stars (Owen & Wu 2017; Owen & Campos Estrada 2019; Rogers et al. 2021); core-powered mass loss, where the residual heat from a planet's formation drives atmospheric escape over time (Ginzburg et al. 2018; Gupta & Schlichting 2019), and giant impacts, in which collisions between planetary bodies strip away portions of the atmosphere or redistribute volatiles (Inamdar & Schlichting 2016; Chance et al. 2022). These mechanisms are discussed in greater detail in Section 5.2.

2.2.2 Compositional Dichotomy

The theory of compositional dichotomy suggests that super-Earths are characterized by a predominantly rocky composition (Carter et al. 2012; Zeng et al. 2016), while sub-Neptunes are believed to be water rich. These sub-Neptunes may have formed outside the ice-line and migrated inwards through type-I migration to the location where we observe them today (Izidoro et al. 2017; Raymond et al. 2018; Chakrabarty & Mulders 2024). The presence of a significant amount of water can explain their large radii (Mordasini et al. 2009; Raymond et al. 2014; Zeng et al. 2016; Venturini et al. 2020).

Planetary formation models suggest that dry cores are unlikely to form and that they are expected to be water rich (Raymond et al. 2005; Bitsch, Bertram et al. 2019a,b). Consequently, these models predict two distinct peaks in planet population: one characteristic of planets with rocky cores and another of planets with water-rich cores (Zeng et al. 2019; Chakrabarty & Mulders 2024). Luque & Pallé (2022) studied transiting exoplanets with radii smaller than $4R_{\oplus}$ around M-dwarf stars and identified a distinct population of water-worlds in the radius-density space. However, this mass-radius distribution of water-rich planets can also be explained by rocky compositions with varying atmospheric content (Rogers et al. 2023).

Model mass-radius relationships suggest a great diversity in internal composition and atmosphere fraction for planets in the super-Earth and sub-Neptune regimes, suggesting a wide range of volatile constituents and compositions (Howard et al. 2012). For example, in a pioneering study, Rogers & Seager (2010) illustrated that the exoplanet GJ 1412 b, with a mass of $6.5M_{\oplus}$ and a radius of $2.5R_{\oplus}$, could have an interior structure that can be explained by at least three qualitatively different compositional end members: a hydrogen-rich gas layer accreted from the protoplanetary nebula, a thick water vapor envelope resulting from the sublimation of ices, or an atmosphere formed by the outgassing of volatiles from the rocky interior. These topics are discussed in greater detail in section 5.1.

2.3 Modelling the Interior Structure of Exoplanets

Precise measurement of mass and radius provide meaningful constraints on the bulk composition, but are limited by data with large uncertainties. Understanding the interior structure of exoplanets is crucial for exploring planetary diversity and determining how unique the Earth is. Interior structure models aim to characterize the radial distribution and composition of a planet's key layers. Despite the large number of detected super-Earths and sub-Neptunes, our understanding of their interior structures remains limited. The materials accreted during planetary formation serve as the building blocks for planets, and their arrangement determines the planet's mass and radius (Mordasini et al. 2011; Alessi et al. 2020). Terrestrial planets primarily consist of a core, mantle, and a thin atmosphere. However, a more generalized planetary structure can include additional layers such as (1) an iron-rich core, (2) a silicate-rich mantle, (3) a water layer, (4) a dense atmosphere of high mean molecular weight gases from interior outgassing, and (5) a light hydrogen/helium-dominated primordial atmosphere accreted from the disk (Sotin et al. 2007). In this section we will discuss, on how the modelling of the planet interior works. We will explore the methods used to model the interior structure of planets and the key factors to consider during the modeling process.

2.3.1 Mass Radius Relation

Mass-radius relations can be derived using planetary interior models, allowing us to establish theoretical trends for different compositions (Seager et al. 2007; Sotin et al. 2007; Fortney et al. 2007; Grasset et al. 2009; Zeng & Sasselov 2013; Lopez & Fortney 2014; Hakim et al. 2018; Haldemann et al. 2020; Otegi et al. 2020). In a mass-radius diagram (Figure 2.6), planets with the same bulk composition align along distinct theoretical curves. These curves serve as an essential reference for interpreting the interior structure of observed exoplanets, providing an initial estimate of their possible compositions and aiding in the study of planetary populations.

Planets that appear above the silicate composition curve must contain substantial amounts of volatile material, such as water or a thick atmosphere, to explain their lower density. According to Rogers (2015) and Otegi et al. (2020), planets with masses exceeding 10 $M_{\oplus}$ and radii above 2 $R_{\oplus}$ tend to follow the trend expected for water-rich planets, implying that they are unlikely to be fully rocky and instead host a substantial volatile layer, possibly in the form of a hydrogen-helium (H/He) envelope. On the other hand, planets that lie near the pure iron curve require a significant fraction of their mass to be in an iron-rich core to account for their high density (Lam et al. 2021; Azevedo Silva et al. 2022). These iron-dominated planets, which resemble Mercury with its large metallic core, are often classified as super-Mercuries.

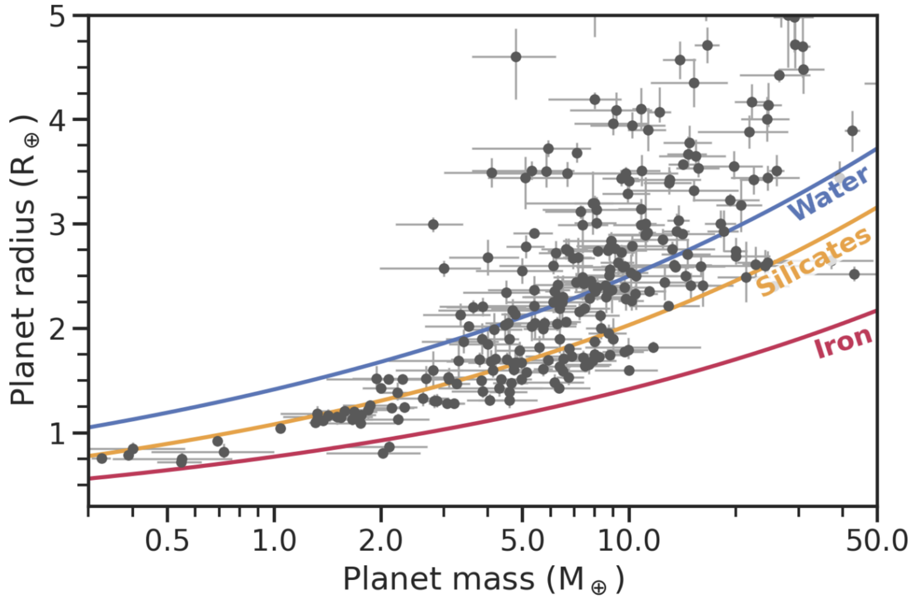

Figure 2.6: Mass-radius diagram for exoplanets below 50 $M_\oplus$. The colored lines mark theoretical mass-radius relations for planets composed of 100% iron (red line), 100% silicates (Earth-like mineralogy, orange line), or 100% water (blue line), all calculated with the TATOOINE model (More details on this model is given in 3.1). Exoplanet data is from the NASA Exoplanet Archive, accessed 2023-06-13 (from (Baumeister 2023))

.

Determining the internal structure of a planet based on mass and radius alone is a highly degenerate problem, as different combinations of core, mantle, and volatile layer compositions can produce similar bulk densities (Valencia et al. 2007; Rogers & Seager 2010). Many of the assumptions made in planetary models significantly impact the predicted radius, yet remain beyond the reach of direct observational constraints. One key factor is the temperature profile, which influences the thickness of volatile layers such as water and atmosphere Thomas & Madhusudhan (2016); Turbet et al. (2020); Nixon & Madhusudhan (2021). Additionally, the presence of light elements in the core lowers its density, meaning that assuming a pure iron core may lead to an overestimation of the planet's mass. For instance, seismic studies show that Earth's core is less dense than pure iron, indicating that 10–15% of its composition consists of lighter elements such as S, Si, O, C, or H (Rama Murthy & Hall 1970; Hirose et al. 2021).

Another uncertainty lies in the mantle composition of exoplanets. Unlike Earth, where mantle composition is inferred from geochemical studies and seismic data, no direct measurements exist for exoplanets, making it difficult to determine their mineralogy. Similarly, the potential existence of surface oceans cannot be inferred from mass-radius measurements alone; additional techniques such as spectroscopic observations are required to confirm their presence (Lustig-Yaeger et al. 2018). The chemical composition of exoplanetary atmospheres remains equally challenging to determine, as detailed spectral characterization is only available for a small subset of planets.

These observational limitations raise intriguing questions about planetary diversity and whether undiscovered types of planets may exist. For example, carbon planets have been hypothesized to form in environments with high carbon-to-oxygen (C/O) ratios, potentially leading to interiors rich in carbides rather than silicates (Kuchner & Seager 2005; Madhusudhan et al. 2011, 2012). Further advancements in observational techniques and theoretical models will be crucial in addressing these uncertainties and refining our understanding of exoplanet interiors.

2.3.2 Degeneracy Problem

Even with precise mass and radius measurements, there are limitations to inferring the interior structure of the planets. For planets with bulk densities lower than a mixture of metal and rock, a degeneracy in volatile content persists (Jontof-Hutter 2019). If transiting exoplanets formed in situ, they are unlikely to contain primordial water, as high-temperature condensation binds oxygen to silicates (Chiang & Laughlin 2013; Chatterjee & Tan 2014). However, if these planets formed farther out in the planetary disk, where water could condense, and subsequently migrated inward, a substantial water component in low-mass planets becomes plausible (Chakrabarty & Mulders 2024).

Constraining the interior structures of exoplanets based on observations is challenging due to the inherent degeneracy in the models; multiple distinct interior compositions and structures can produce the same observable properties, such as mass and radius, making it difficult to uniquely determine a planet's internal composition (Seager et al. 2007). Various methods have been proposed to overcome this issue. Valencia et al. (2007) introduced ternary diagrams to constrain the interior composition of super-Earths without gas envelopes. Zeng & Seager (2008) presented description of the functional form of the ternary diagram interior composition curves. Rogers & Seager (2010) pioneered the use of this method to quantify the interior structure of super-Earth and sub-Neptunes based on mass and radius measurements. Subsequently studies by Schmitt et al. (2014) and Weiss & Marcy (2014) were built on this work, though they were highly limited to only two or three parameter space and required strong prior assumption such as rocky composition for super-Earth. Dorn et al. (2015) advanced this approach by applying Bayesian inference to constrain interior structure of rocky exoplanets, using mass, radius and stellar elemental abundance data. This was later extended by Dorn et al. (2016) to include volatiles (liquid and high pressure ices and gaseous layer) for super-Earth and sub-Neptunes. They employed a Bayesian inference method that allowed for the estimation of these volatile layers without imposing strong prior constraints on their properties. Through Bayesian inference using Markov Chain Monte Carlo (MCMC) technique (Scott 2010), we can get probabilistic inferences about the interior structure and composition of planets—including the core, mantle, ice, ocean, and gaseous layers—while effectively quantifying the inherent degeneracy in the models.

2.3.3 Stellar Abundance

Apart from volatiles, Earth's composition of refractory elements closely matches that of chondritic meteorites, which in turn resemble the elemental abundances of the Sun's photosphere (Brown 1950). However, rocky planets do not necessarily share Earth's composition if their host star has different abundance ratios of elements like Fe, Si, Mg, C and O compared to the Sun (Bond et al. 2010). For instance, the high bulk density of Mercury suggests that planet's composition can differ significantly from that of its host star. These implies the possibility of a wide variety of plausible compositions for rocky planets. Observations alone cannot confirm the core compositions of planets, making it difficult to distinguish between bare water-rich planet and one with rocky core with a thin atmosphere (Seager et al. 2007; Fortney et al. 2007; Rogers & Seager 2010).

Planets formed in-situ are expected to lack primordial water, as oxygen binds with silicates in the high-temperature regions of the disk (Chiang & Laughlin 2013). However, planets formed beyond the water-ice line can eventually migrate inward, retaining substantial amount of water, even in low-mass exoplanets. Rogers (2015) suggested that most planets around 1.6 $R_\oplus$ have densities too low to be composed solely of iron and silicates, indicating that diversity of super- Earth could be greater than previously thought. Super-Earth are found in various stellar systems with diverse metallicities and elemental abundances (Buchhave & Latham 2015). These difference in chemical composition can lead to different formation scenarios for super Earth (Bitsch & Johansen 2016). The diversity in densities of low mass exoplanets points at high degree of variation in their interior structures (Jontof-Hutter 2019).

2.4 Motivation of my Research

Inherent degeneracies in exoplanet interior structure models necessitate additional constraints on parameters. This can be achieved by introducing new parameters or refining existing ones. Focusing on water and gas layers is particularly important, as these components significantly influence radius measurements. Refining these parameters is crucial for future missions aimed at detecting exoplanets, especially low-mass ones, due to their abundance and implications for habitability. The objective of this work is to investigate how varying the constraints and a priori assumptions on the interior structure of low mass exoplanets - particularly on the presence of volatiles - affects the degeneracy of interior predictions.

Methodology

In this study, we combine physical modeling with machine learning to investigate the internal structures of low-mass exoplanets. The code TATOOINE serves as the foundational model, generating synthetic data on the radial structure of planets by applying physical laws such as hydrostatic equilibrium, mass continuity, and equations of state (EoS). This dataset provides detailed insights into planetary compositions. Trained on TATOOINE's data, the machine-learning-based model ExoMDN predicts exoplanet interior structures from observable parameters like mass, radius, and equilibrium temperature. In addition, ExoMDN efficiently examines how constraints on the abundance of volatiles influence the distribution of possible interior layers. The following sections introduce the methodologies used in this study.

3.1 TATOOINE: Toolkit for ATmospheres and Obtaining Optimal Interiors of Exoplanets

The TATOOINE (Tool for ATmospheres, Outgassing, and Optimal INteriors of Exoplanets) code (Baumeister et al. 2020) is a 1D model specifically developed to calculate the radial structure of low-mass exoplanets. Based on interior models such as those by Sotin et al. (2007) and Valencia et al. (2007), TATOOINE simulates a planet's interior as a series of compositionally-distinct layers, each governed by its own Equation of State (EoS). To model the interior structure of exoplanets using the TATOOINE code, several input parameters are required, including planetary mass, layer mass fractions, boundary conditions (BCs), and EoS. These inputs provide the foundation for the numerical integration process, where the coupled differential equations for mass conservation, hydrostatic equilibrium , and material density, described by suitable EoS, are solved. The integration starts at the planet's surface and proceeds inward, with layer boundaries being adjusted according to the specified BCs. These BCs are crucial for defining transitions between different layers within the planet, such as the fraction of the total mass allocated to each layer, pressure thresholds at which layer transitions occur , and temperature effects that influence phase changes and material transitions. To ensure the accuracy of the model, convergence criteria are applied, including the requirement that the mass profile converges to zero at the planet's center. This process uses the Brent's method (Brent 1972), a root-finding algorithm, to accurately solve the equations describing the planet's internal structure.

The code provides key outputs such as planet's outer radius, layer thicknesses, and profiles of the planet's interior like pressure, density, temperature and gravity. With its adaptable design, TATOOINE can model a wide range of planetary compositions and structures by adjusting EoS parameters and BCs. This flexibility makes it a powerful tool for the rapid and precise characterization of diverse exoplanet interiors. An overview of the TATOOINE modeling process is shown in Figure 3.1. Hydrostatic equilibrium is achieved when the inward gravitational force is balanced by the outward pressure gradient. This equilibrium is described by the following equation:

$$\frac{dP}{dr} = -\frac{GM(r)\rho(r)}{r^2}, \tag{3.1}$$

where P is the pressure, r is the radial distance from the center, G is the gravitational constant, $M(r)$ is the mass enclosed within radius r, and $\rho(r)$ is the density. The continuity equation, which ensures mass conservation within the planet, is given by:

$$\frac{dM}{dr} = 4\pi r^2 \rho(r). \tag{3.2}$$

This equation relates the incremental change in mass, dM, to the density and radial distance. The EoS describes how the pressure varies within each compositional layer of a planet, depending on the density, temperature (T), and composition c at a given radial distance. This relationship is expressed as: $P(r) = f(\rho(r), T(r), c(r))$ where f represents the functional form of the EoS specific to each layer's materials demonstrated in Figure 3.2. Accurate EoS data are essential for predicting the distribution of materials within a planet and understanding phase transitions across its layers. In our model, the equation of state (EoS) used for each layer is detailed in the subsections below.

TATOOINE employs a straightforward 1D numerical integration method that links observable characteristics, such as radius, to internal parameters like core mass and chemical composition. This approach is a forward model that is conceptually simple to solve and provides a direct way to predict planetary interiors based on given input parameters. However, the goal is to use observable properties—such as planetary mass, radius, and equilibrium temperature—to infer the interior structure, which poses an inverse problem. Solving this inverse problem can lead to highly degenerate solutions and often requires computationally intensive sampling of the parameter space for each individual planet.

3.1.1 Equations of State

TATOOINE utilizes specific EoS for each compositional layer to represent the physical and thermodynamic properties of the planet's interior. Each layer – metallic core, silicate mantle, water, and gas layer – is modeled with dedicated EoS, which are described in the following subsections.

Iron Core

The core is assumed to consist of pure, solid hcp-iron. It is modeled using an temperature-dependent, high pressure EoS. For pressures below 234.4 GPa, the EoS by Bouchet et al. (2013)

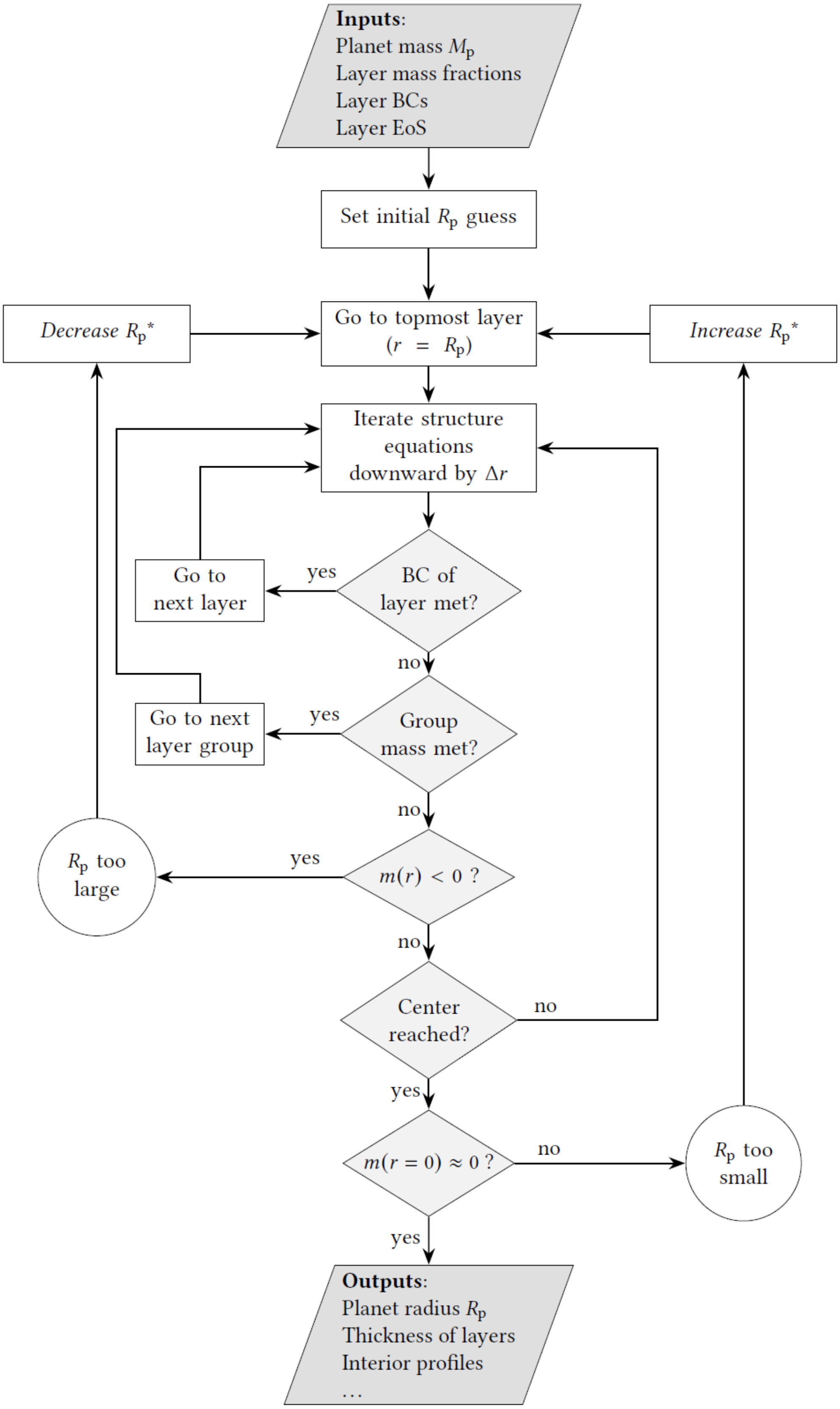

Figure 3.1: Flowchart for the iterative process of determining planetary radius and interior structure(fromBaumeister (2023)).

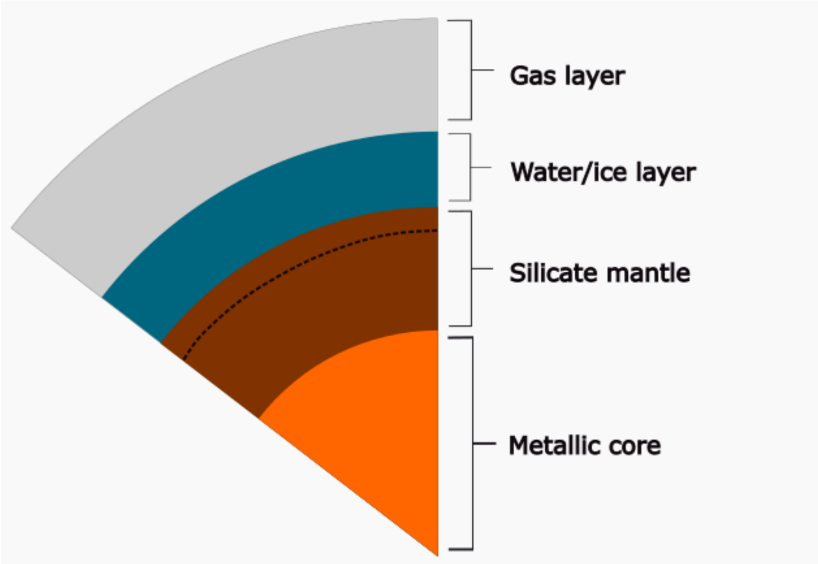

Figure 3.2: Schematic representation of the interior structure of a low-mass exoplanet, as used in the ExoMDN model. The diagram illustrates a metallic core at the center, surrounded by a silicate mantle, which is divided into an upper and lower mantle (separated by a dashed line). Above the mantle lies a water/ice layer, followed by an outer gaseous layer, representing a possible hydrogen-helium atmosphere.

is used. At higher pressures, the model transitions to the high-pressure EoS from Hakim et al. (2018) and is valid up to 10 TPa.

The presence of light elements such as sulfur, silicon, hydrogen or oxygen in the core can significantly affect its density and therefore the planet radius (Hakim et al. 2018). The abundance of light elements in the core is highly influenced by core formation processes, magma ocean cooling, and the initial distribution of light elements in the protoplanetary disk (Hirose et al. 2021). However, constraining the exact amount of light elements in the core is challenging. To address this, the amount of light elements is often treated as a free parameter, which can increase the degeneracy of the model. In the training set used by ExoMDN, the contribution of light elements in the core is neglected for simplicity, a common practice in exoplanet interior modeling (Seager et al. 2007).

Silicate Mantle

The silicate mantle is divided into an upper and lower mantle. The upper mantle consists primarily of minerals such as olivine $(Mg, Fe)_2SiO_4$ and pyroxene $(Mg, Fe)_2Si_2O_6$, while the lower mantle is composed of magnesiowüstite (Mg, Fe)O, bridgmanite $(Mg, Fe)SiO_3$, and, at high pressure, a magnesiowüstite/post-perovskite phase. The upper to lower mantle transition is assumed to occur at a fixed pressure of 23 GPa, and the post-perovskite transition is given at a temperature-dependent pressure level of:

$$P(T) = 89.184\,\mathrm{GPa} + 13.3\,\mathrm{MPa\,K^{-1}} \cdot T \quad (3.3)$$

where T is the adiabatic temperature in the mantle, as specified by Tateno et al. (2009). The upper and lower mantle are modeled using a modified Tait EoS from Holland & Powell (2011), while the post-perovskite phase is treated with a generalized Rydberg EoS from Wagner et al. (2011).

In general, the mantle composition could be chosen according to the elemental abundances measured int the parent star (Dorn et al. 2016). However, the relationship between stellar metallicity and planetary compositions is complex and not straightforward (Plotnykov & Valencia 2020). Therefore, for simplicity, the composition of the silicate mantle is assumed to match that of Earth's mantle, with a molar Mg/Si ratio of 1.131 and a magnesium number (Mg#) of 0.9 (Sotin et al. 2007). The Mg/Si ratio determines the proportion of minerals in the mantle, while the magnesium number (Mg#) represents the ratio of Mg to Fe end-members.

Water layer

The water layer is modeled using the tabulated AQUA EoS from Haldemann et al. (2020), which covers water in multiple phases—gas, liquid, and solid—and accounts for its behavior under a range of pressures and temperatures. For any given temperature and pressure, the liquid and solid layers are assumed to be fully convective, with the adiabatic temperature profile calculated using the adiabatic gradient provided in the AQUA table. At equilibrium temperature, the water vapor is assumed to be part of the isothermal atmosphere (see below).

Atmosphere

The low densities observed in many exoplanets suggest the presence of extended–possibly primordial–envelopes composed of hydrogen and helium (Jontof-Hutter 2019). The interior model thus includes an outer gaseous H/He envelope with a solar-like composition (71% hydrogen and 29% helium by mass) that is treated with the EoS from Saumon et al. (1995). The atmosphere is simply assumed to be isothermal, with its temperature set equal to the planetary equilibrium temperature, following the approach used in previous studies (Dorn et al. 2016; Zeng et al. 2019). While such a simple treatment of the atmosphere does not capture important temperature variations that may also affect interior model predictions, more detailed models would require including additional parameters, such as infrared and optical opacities, and the planet's intrinsic temperature (Guillot 2010). Although this more sophisticated treatment of the atmosphere is possible with TATOOINE, it would render difficult the generation of a suitable training set for the machine learning model that we employed.

3.2 Machine Learning in Planetary Science

Recently, machine learning has gained a special place in the scientific community due to the vast availability of data. In exoplanetary science, it is utilized for tasks ranging from detecting transit signals in large datasets of light curves (Shallue & Vanderburg 2018; Chaushev et al. 2019; Armstrong et al. 2020; Tey et al. 2023) to predicting efficiently the interior structures of the planets (Baumeister et al. 2020; Baumeister & Tosi 2023; Zhao et al. 2024). Chaushev et al. (2019) employed Convolution Neural Network(CNN) to classify planets from the Next Generation Transiting Survey(NGTS). Surrogate machine learning methods have been applied in various planet formation models (Alibert & Venturini 2019), mantle convection simulations

(Agarwal et al. 2020), and in the study of evolution of atmosphere due to mass loss (Rogers et al. 2023).

Machine learning can also be effectively employed for rapid inference of planetary interiors. Conventional methods like MCMC and generalized Bayesian inference require around ten to thousands runs to be performed for each individual planet (Rogers & Seager 2010; Dorn et al. 2016, 2017). By generating a large dataset of planets with different interior structures, machine learning can be trained to infer the relationships between mass, radius and other observables. This approach allows exploring various combinations of interior structures without the need for running computationally expensive forward model like MCMC.

3.3 ExoMDN

ExoMDN (Exoplanet Mixture Density Network) by Baumeister & Tosi (2023) is a machine-learning model developed to rapidly infer the interior structure of exoplanets based on observable parameters such as mass, radius, equilibrium temperature, and tidal Love number k_2 (Padovan et al. 2018; Csizmadia et al. 2019; Hellard et al. 2019). This models is specifically designed to address the computational challenges associated with traditional sampling methods like MCMC method. ExoMDN uses so-called mixture density networks (Bishop 1994) – a special type of neural networks trained to predict probability distributions in the form of mixtures of multiple Gaussian functions to infer the distribution of possible interior compositions for a given set of observables. ExoMDN is trained on a large set of interior structures pre-calculated with the TATOOINE code and spanning a wide range of compositions (including iron cores, silicate mantles, water layers, and gaseous atmospheres). ExoMDN offers an efficient approach to modeling low-mass exoplanets' interiors in seconds.

3.3.1 Training Data and Network Architecture

ExoMDN was trained with a dataset consisting of 5.6 million synthetic interior structures calculated with TATOOINE by randomly sampling from prior distributions of the layer mass fractions. The planet samples have masses ranging from 0.1 to $25 M_{\oplus}$ and equilibrium temperatures from 100 to 1000 K (see Table 3.1). The mass fractions of each planetary layer were normalized to sum to one. All the mass fractions, except for the gas layer, were sampled uniformly. The lower limit of w_{Gas} is set to 10^{-8} because the dataset does not contain runs where these fractions are exactly zero.

The mass and radius fractions were log-transformed to enable the prediction of multivariate distributions. This log-ratio transformation was used to handle the special nature of compositional data, where the mass fractions of all planetary layers must sum to one. By converting the data into logarithmic ratios, the model can better manage the relationships and variability between the different layers. This approach ensures that the predictions remain physically consistent while improving the model's ability to capture complex patterns in the data. A schematic representation of the ExoMDN model is shown in Figure 3.3. The model takes observable parameters, including planetary mass (M_p), radius (R_p), equilibrium temperature (T_{eq}), and an optional fluid Love number (k_2) as inputs. In this work, the fluid number (k_2) is not considered. These inputs pass through multiple hidden layers to produce mixture parameters of Gaussian distributions: mixing weights (α_i), means (μ_i), and variances (σ_i). The resulting posterior mixture distribution, represented in log-ratio space, is transformed into compositional space, providing a probabilistic distribution of possible interior structures for the planet (Baumeister & Tosi 2023).

Parameter	Range
M_p	$0.1 - 25\,M_\oplus$
T_{eq}	$100 - 1000\,\text{K}$
w_{Core}	$0 - 1$
w_{Mantle}	$0 - 1$
w_{Water}	$0 - 1$
w_{Gas}	$10^{-8} - 1$

Table 3.1: Parameter ranges used in the model. M_p represents the planetary mass in Earth masses ($M_\oplus$), T_{eq} is the equilibrium temperature in Kelvin, and w_{Core}, w_{Mantle}, w_{Water}, and w_{Gas} are the mass fractions of the core, mantle, water, and gas layers, respectively. The gas mass fraction (w_{Gas}) has a lower limit of 10^{-8} due to dataset limitations.

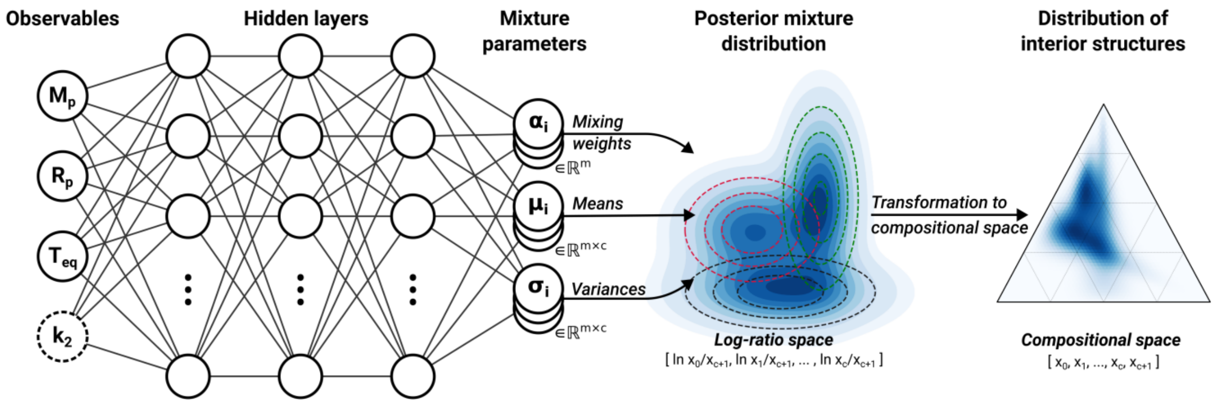

Figure 3.3: Schematic representation of the ExoMDN model.

3.3.2 Composition of an Earth-like Planet

The interior composition of a $1M_\oplus$, $1R_\oplus$ planet, such as Earth, is not necessarily limited to metal and rock. In the absence of additional constraints, the presence of significant amounts of volatiles, such as water and gas, can lead to a much broader range of potential interior structures. Even for a dense planet like Earth, various combinations of core, mantle, water, and gas layers can satisfy the observed mass and radius. This highlights the inherent degeneracy in interior structure predictions based solely on limited observables like mass, radius, and equilibrium temperature.

To investigate this degeneracy, the ExoMDN model was used to predict the posterior distribution of potential interior layer thicknesses for an Earth-like planet, as shown in Figure 3.4. The model uses log-ratio transformations to approximate the posterior distribution in a six-dimensional space, encompassing the thickness and mass fractions of the core, mantle, water, and gas layers. For clarity, we focus on the thickness fractions of the layers. A total of 200,000 points were sampled from the log-ratio distribution to construct the posterior distribution shown in Figure 3.4. The diagonal plots represent the marginal distributions for each layer thickness, while the off-diagonal plots illustrate the relationships between pairs of layers. The blue dashed lines on the diagonal plots mark the median values for each distribution, and the dotted lines indicate the 5th and 95th percentiles. Additionally, three end-member interior structures are highlighted with colored symbols, representing distinct possible solutions under the given constraints.

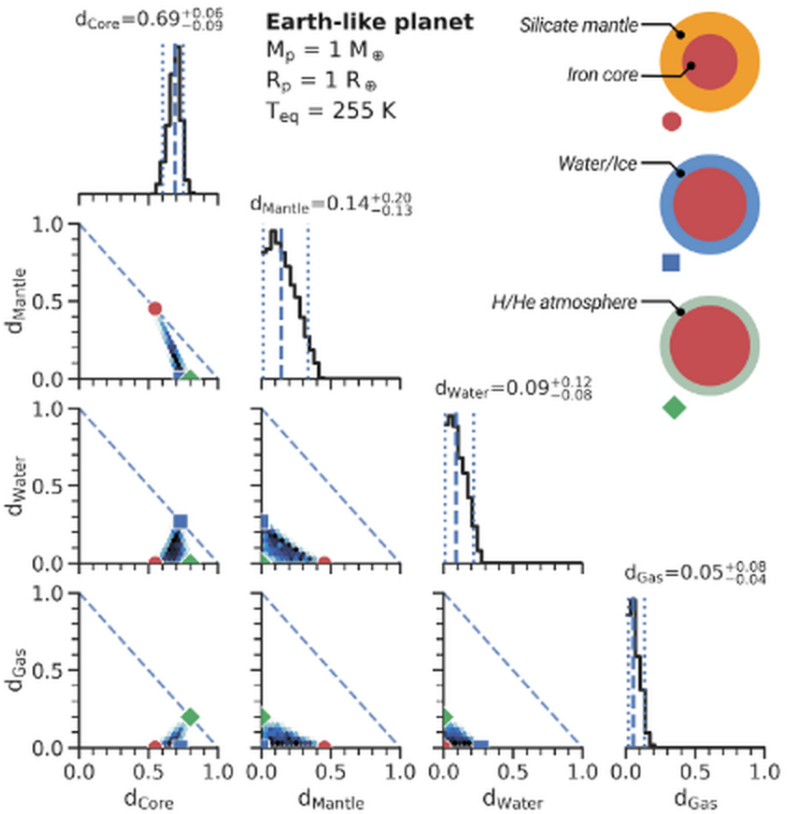

Figure 3.4: Predicted thickness of interior layers for an Earth-like planet with $1M_\oplus$ and $1R_\oplus$. The colored points mark possible end-member compositions, which are illustrated on the right. The red circle corresponds to the solution that is closest to Earth's true interior structure. The diagonal plots show the marginal distributions of each layer, with the blue dashed lines marking the median value and the dotted lines the 5th and 95th percentiles (from(Baumeister & Tosi 2023)).

The plot highlights three end-member interior structures with two layers, represented by three different colors. These end-members are sampled from the posterior distribution and illustrate distinct combinations of planetary layers that satisfy the observed mass and radius. The first is Earth's actual structure, comprising an iron core that makes up 55% of the planet's radius, with a silicate mantle on top. The second is an iron-water structure, where the core con-

Parameter	Range
M_p	$0.1 - 25\,M_\oplus$
T_{eq}	$100 - 1000\,\text{K}$
w_{Core}	$0 - 1$
w_{Mantle}	$0 - 1$
w_{water}	$w_{\text{water}}^{\text{min}} - w_{\text{water}}^{\text{max}}$
w_{Gas}	$w_{\text{gas}}^{\text{min}} - w_{\text{gas}}^{\text{max}}$

Table 3.2: Parameter ranges utilized in the new approach. The ranges for w_{water} and w_{gas} are specified as $w_{\text{water}}^{\text{min}} - w_{\text{water}}^{\text{max}}$ and $w_{\text{gas}}^{\text{min}} - w_{\text{gas}}^{\text{max}}$, respectively, and are determined based on specific constraints from the dataset.

stitutes 73% of the planet's radius, with an ice layer making up the rest. The third is an iron-gas structure, characterized by a massive iron core constituting 80% of the planet's radius, with a gaseous envelope occupying the rest. In cases 2 and 3, the iron core is much larger to compensate for the low densities of the water and gas layers. Although these two cases are unlikely to occur in nature, they highlight the difficulty of fully constraining the interior structure without additional information. The figure also presents the marginal distributions for each layer thickness along the diagonal panels, showing the range of possible solutions. For example, the core layer's marginal distribution is tightly peaked around high values, reflecting its dominance in most solutions. In contrast, the mantle, water, and gas distributions exhibit broader ranges, indicating less constraint on these layers in the absence of additional information. The off-diagonal panels highlight correlations between different layers, such as the inverse relationship between core thickness and the contributions of water and gas, as a larger core compensates for the lower densities of volatile layers. In this example, the thickness of the silicate mantle, in particular, is poorly constrained.

Earth's actual interior, with a core radius fraction of 55%, lies just marginally outside the bulk of the predicted distribution. This finding aligns with the first solution highlighted in the plot, corresponding to the actual structure of Earth. However, this marginal offset underscores the inherent degeneracy in interior structure predictions derived from limited observables like mass and radius, highlighting the need for further constraints to improve accuracy.

3.4 Constrained Interior Predictions

The retrieval of exoplanet interiors is inherently degenerate due to the vast range of potential compositions that can produce the same observed mass, radius, and equilibrium temperature. This degeneracy is particularly significant for volatile layers, such as water (w_{Water}) and gas (w_{Gas}), which have low densities and contribute disproportionately to the planetary radius. Their large volume contribution compared to the denser, core and mantle further complicates the determination of interior structures, often resulting in widely varying solutions.

To address this issue, I propose a new approach that introduces more constraints on water w_{Water} and gas w_{Gas} mass fraction. These constraints will enable us to reduce the space of possible interior solutions, enabling less degenerate predictions of interior configurations of exoplanets.

The revised parameter ranges are presented in Table 3.2.The constrained ranges for w_{water} and w_{gas}, denoted as $w_{\text{water}}^{\text{min}} - w_{\text{water}}^{\text{max}}$ and $w_{\text{gas}}^{\text{min}} - w_{\text{gas}}^{\text{max}}$, respectively, represent the minimum and maximum plausible amounts of water and gas that a planet could contain, given its mass, radius, and equilibrium temperature as predicted by ExoMDN. In this thesis, this approach is referred to as the "constrained prediction scenario."

By applying these constraints on water and gas layers, the parameter space is effectively narrowed, allowing for a more focused exploration of physically plausible solutions. Specifically, "maximum constraints" correspond to scenarios where water and gas are at their minimum values (w_{min}), while "minimum constraints" correspond to scenarios where water and gas are at their maximum values (w_{max}). This approach not only limits the degeneracy inherent in interior predictions but also provides a more realistic basis for studying the structure of low-mass exoplanets.

Data Analysis & Results

The ExoMDN model utilizes machine learning to predict exoplanet interior structures based on observed parameters like mass, radius and equilibrium temperature. This model allows for a significant reduction in computational costs, which would otherwise be extremely high due to the need to evaluate tens of thousands of potential interior configurations for a single planet. These configurations involve varying combinations of core, mantle, water, and atmospheric gas layers. By utilizing ExoMDN, it becomes possible to efficiently explore the posterior distributions of planetary interiors under various constraints on volatile content, such as water and gas, enabling deeper insights into their composition and structure.

In this section, we present a detailed analysis of planetary interior structures, beginning with Earth and extending to Moon-like, Earth-like and Mercury-like compositions across different planet masses within the low-mass exoplanet regime. We explore how constraints on the low-density water and gas layers influence predictions of the core radius fraction (or of the mass fraction as shown in Appendix 7). Additionally, we examine the impact of observational uncertainties on these constraints, with particular emphasis on the expected accuracy of mass and radius measurements from the upcoming PLATO mission (Rauer et al. 2014).

4.1 Constrained Predictions for an Earth-like Planet

To understand the effects of water and gas layers upon constraining the core (or mass) radius fraction of a planet, first, I carried out a series of constrained predictions for an Earth-like planet using ExoMDN. In this context, a constrained prediction involves limiting the parameter space of possible water and gas layer thicknesses based on mathematically admissible bounds derived from my model predictions. These maximum and minimum values define the upper and lower bounds of the x-axis and y-axes in Figure 4.1, respectively.

For each combination of d_{water} and d_{gas} within this range, starting from a minimum value (determined by physical limitations and numerical resolution), I carried out a full prediction of the posterior distribution of the planet's interior structure. Then, I calculated the median of the core radius fraction for each prediction. Figure 4.1 illustrates the relationship between core radius fraction under different constraints on water and gas content for an Earth-like planet ($1R_\oplus$ and $1M_\oplus$, $T_{\text{eq}} = 255\text{K}$), as generated by the ExoMDN model. Each point on the plot corresponds to a specific posterior distribution of the planet's interior structure, which includes core, mantle, water, and gas layers. The x-axis represents increasing water content from left to right, while the y-axis represents increasing atmospheric content from bottom to top. The color bar indicates the varying core radius fraction, ranging from 57% to 68%. The figure specifically presents the median of the core radius fraction (d_{core}) derived from these posterior distributions.

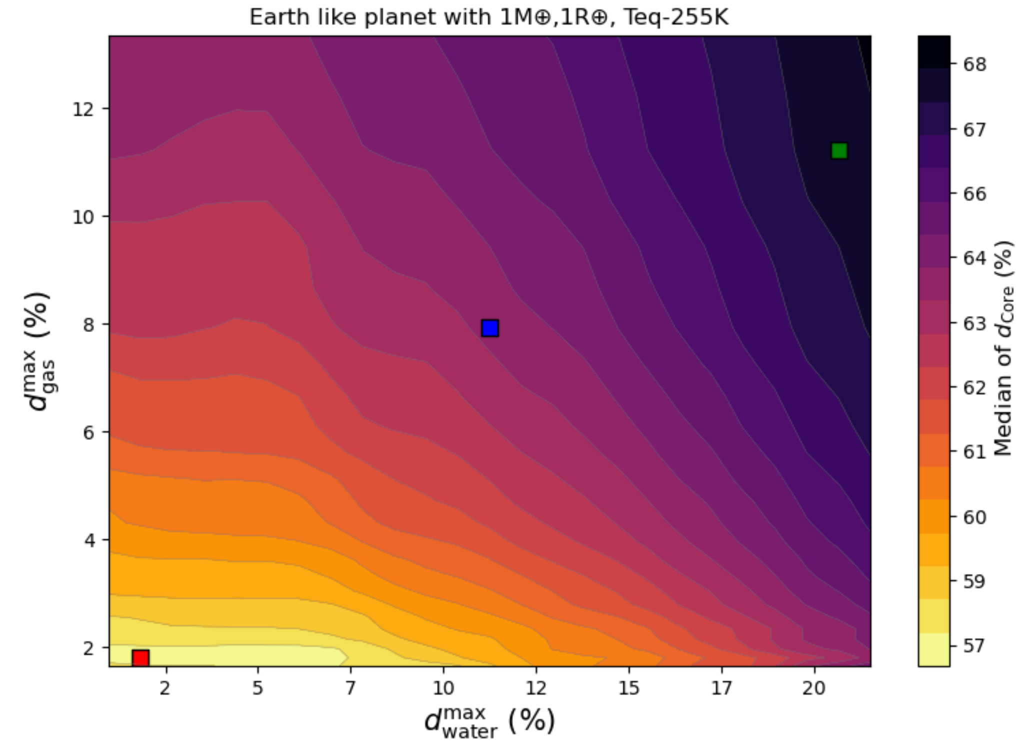

Figure 4.1: Median of the distribution of core radius fractions (d_{core}) as a function of maximum water ($d_{\mathrm{water}}^{\mathrm{max}}$) and gas ($d_{\mathrm{gas}}^{\mathrm{max}}$) content for an Earth-like planet ($1R_{\oplus}$, $1M_{\oplus}$, $T_{\mathrm{eq}} = 255$ K), generated using the ExoMDN model. The x-axis represents increasing water content, and the y-axis represents increasing atmospheric content. The minimum constraints scenario (green square) represents a volatile-rich case where the planet has (close to) the highest allowed water and atmospheric content, leading to the largest possible core radius fraction. The moderate constraints scenario (blue square) corresponds to an intermediate case, where we allow a moderate amount of water and gas. Finally, the maximum constraints scenario (red square) represents a volatile-poor case, where the least amount of water and gas is allowed, resulting in the lowest core radius fraction.

In regions where both water and gas content are set to their possible maximum values (indicated by the green square in Figure 4.1, representing minimum constraints case), the core radius fraction reaches up to 68%. This suggests that planets with higher volatile content can have significantly different internal structures compared to rocky planets like Earth despite having the same bulk density. The increasing core radius fraction in the volatile-rich scenarios indicates that the core fraction becomes less and less constrained as the amount of water and gas content increases. The posterior distribution for the case with maximum water and maximum gas is illustrated in Figure 4.2a. We can also observe that the distribution is more spread out, indicating greater flexibility and less constraint on the core radius fraction.

As we move towards scenarios with moderate constraints on water and gas (indicated by

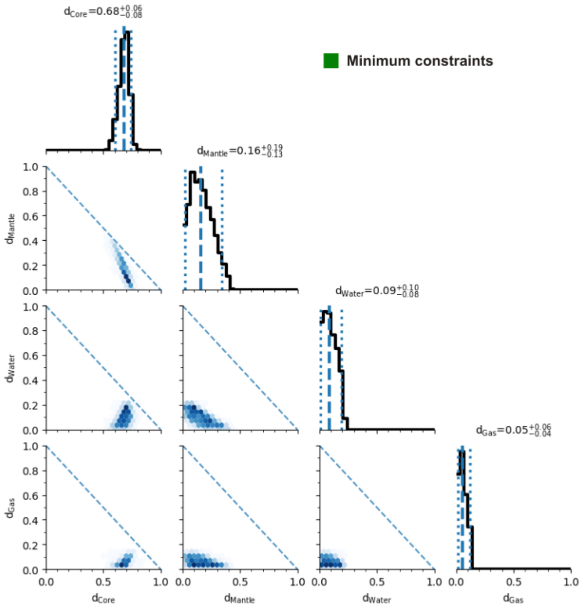

(a) Minimum Constraints

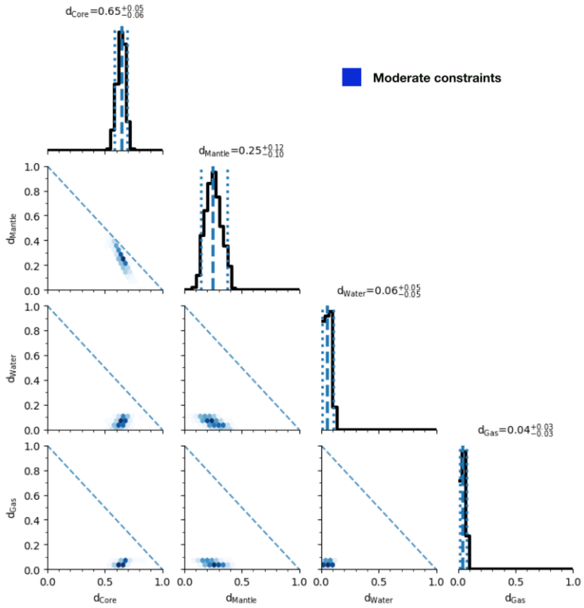

(b) Moderate Constraints

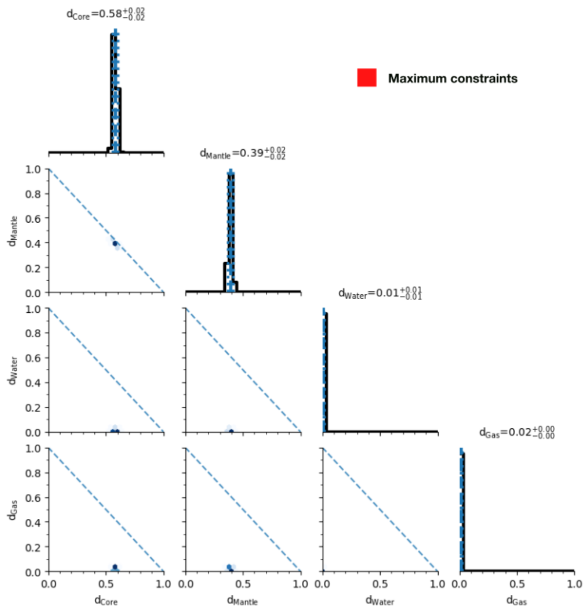

(c) Maximum Constraints

Figure 4.2: Posterior distribution of interior layers under different constraints for an Earth-like planet. The plots represent: (a) Minimum Constraints (green), where the water and atmospheric content are set close to their maximum possible value and allowed to vary freely within the broadest possible range; (b) Moderate Constraints (blue), where an intermediate amount of water and gas is permitted; and (c) Maximum Constraints (red), where the water and gas content are set close to their lowest possible values. These constraints influence the inferred core radius fraction, with maximum constraints leading to more precise predictions. The colored squares correspond to those indicated in the contour plot 4.1.

the blue square in Figure 4.1), the median of the core radius fraction decreases slightly, representing a more intermediate structure. These moderate constraints result in a core radius fraction that is still elevated compared to Earth, but significantly lower than in the minimum constrained scenario, showing that varying levels of volatiles can still lead to different internal compositions. The posterior distribution of the core thickness for this moderately constrained scenario is shown in Figure 4.2b.

Finally, in regions where both water and gas content are minimal (indicated by the red square in Figure 4.1, representing maximum constraints), the core radius fraction is approximately 57%, which is only slightly higher than Earth's actual core radius fraction of 55%. This small difference arises due to the inclusion of a minimal amount of water and gas in the model. In this scenario, the model closely replicates Earth's internal structure, suggesting that the core radius fraction is well-constrained when the volatile content is low. The posterior distribution for this case is shown in 4.2c, suggesting that even small variations in water and gas can substantially alter the internal structure of the planet.

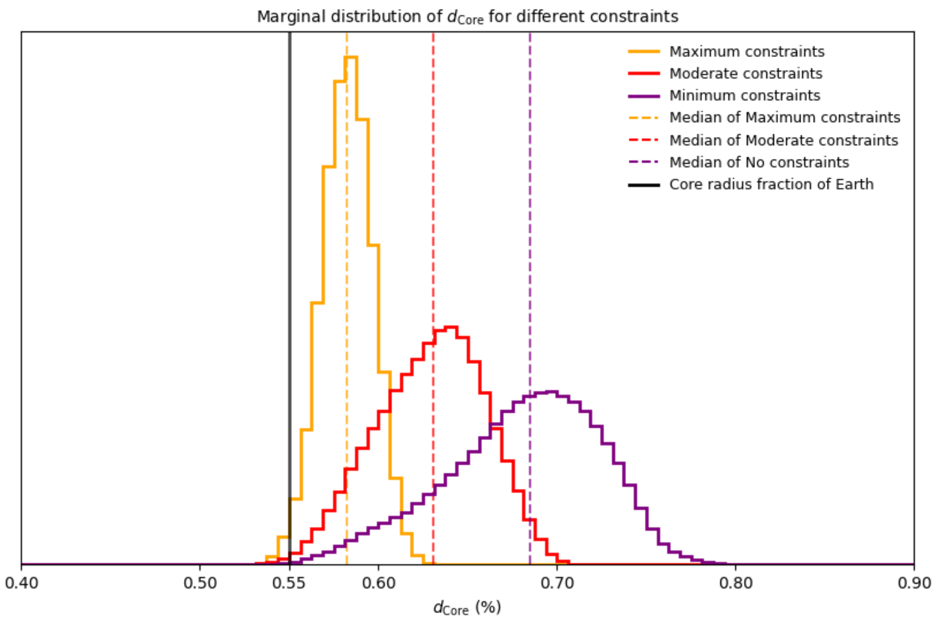

Figure 4.3: Marginal distributions of the core radius fraction (d_{core}) for an Earth planet with $1M\oplus$ and $1R\oplus$ under different constraints. The distributions illustrate how the core size fraction varies under maximum constraints, moderate constraints, and minimum constraints, with the median values indicated for each scenario. The core radius fraction of Earth (marked in black) is shown for comparison and aligns more closely with the distribution under maximum constraints.

In summary, this plot, along with corresponding posterior distribution plots, provide a clear visual representation of how varying water and gas content affects the core radius fraction. Tighter constraints on these volatile components lead to more accurate estimates of a planet's internal composition, particularly for low-mass, rocky exoplanets. The model effectively captures the range of possible internal structures, from predominantly rocky to volatile-rich compositions.

Figure 4.3 compares the marginal distributions of the (d_{core}) for a planet with $1 R_{\oplus}$ and $1 M_{\oplus}$ under varying constraints: minimum constraints, moderate constraints, and maximum constraints. The distribution for minimum constraints is the broadest, centered around $d_{\text{core}} \approx 0.70$, allowing for a wide range of possible core sizes. In contrast, the distribution under maximum constraints is the narrowest, peaking around $d_{\text{core}} \approx 0.57$, indicating a more restricted core size range. Moderate constraints fall between these two, with a peak around $d_{\text{core}} \approx 0.64$. The median values of the distributions shift left as constraints tighten, with the core radius fraction of Earth ($d_{\text{core}} \approx 0.55$) aligning closely with the maximum constraints. This suggests Earth's internal structure is more consistent with stricter compositional limitations, likely influenced by specific water of gas content. This plot underscores the importance of constraining water and gas on planets to get the core radius fraction of low-mass planets.

4.2 Mass-Radius Diagram for Different Compositions

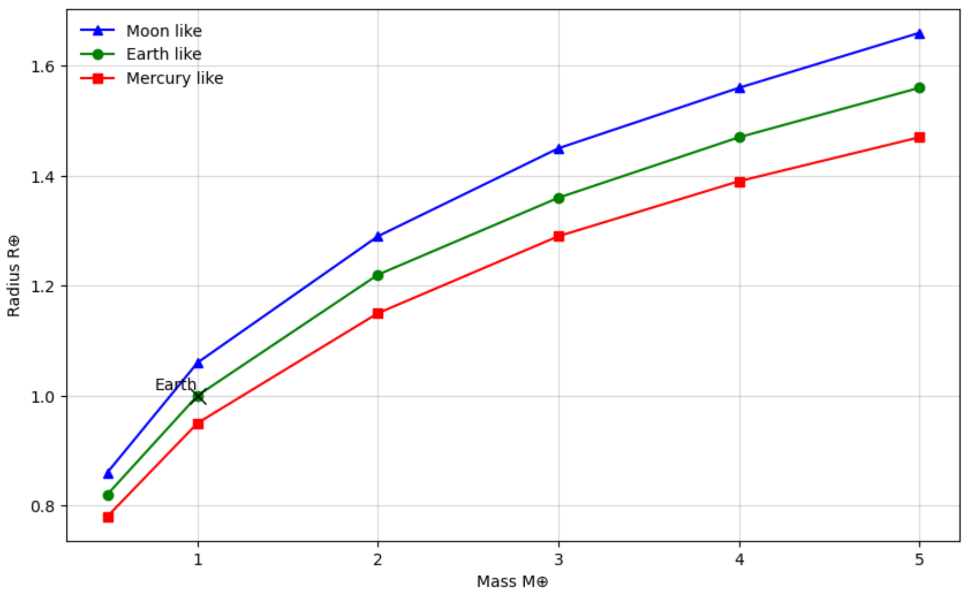

Figure 4.4: Mass-radius (M-R) diagram comparing Moon-like, Earth-like, and Mercury-like planets. The X-axis shows planetary mass in Earth masses ($M_{\oplus}$), and the Y-axis shows planetary radius in Earth radii ($R_{\oplus}$). The curves demonstrate how planetary radius increases with mass for different compositions: Moon-like (blue), Earth-like (green), and Mercury-like (red).

To study the constraints on water and gas content in planets of varying mass and composition, it is essential to calculate the so-called mass-radius relations. These relations have been explored early on by studies such as Valencia et al. (2006); Sotin et al. (2007); Fortney et al. (2007); Seager et al. (2007). In this study, mass-radius relations are calculated using the TATOOINE code, assuming a simple two-layer structure consisting of an iron core and a rocky mantle for Earth-like, Mercury-like, and Moon-like planets. Core radius fractions are set to 20% for the Moon, 55% for Earth and 70% for Mercury with planet masses ranging from 0.5 to 5 $M_{\oplus}$ and is shown in Figure 4.4.

Planets with Moon-like compositions tend to have larger radii for a given mass due to their low iron content and lower density. Earth-like planets, represented by the middle curve, reflect a moderate core fraction, resulting in intermediate radii. In contrast, Mercury-like planets have smaller radii for the same mass due to their large iron content and higher density.

4.3 Constrained Predictions for Planets with Earth-like Composition

Based on the above mass-radius relations, we can use ExoMDN to investigate the possible internal structures of planets with Earth-like composition up to 5 $M_\oplus$. For each planetary mass, the contour plots in Figure 4.5 show how the median of the distribution of the core radius fraction (d_{core}) varies as a function of the maximum allowed water and gas fractions, assuming an Earth-like composition. For low-mass planets, the core radius fraction remains relatively high when water and gas contributions are small, which corresponds to the bottom-left region of each of the contour plot.

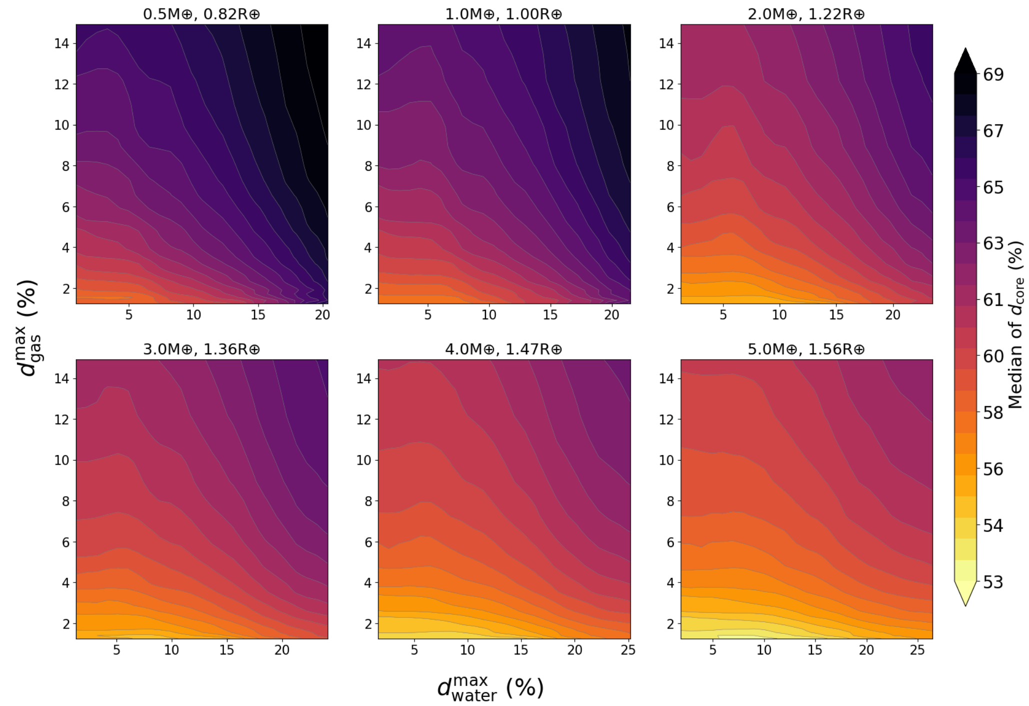

Figure 4.5: The core radius fraction (d_{core}) as a function of water and gas fractions for planets with Earth-like composition with masses ranging from 0.5 to 5$M_\oplus$. Each panel represents a different planetary mass, with the core radius fraction varying as a function of the maximum allowed water (d_{water}) and gas (d_{gas}) fractions.

As planetary mass increases, the core radius fraction decreases, reflecting the planet's capacity to hold greater amounts of volatiles, such as water and gas, which reduces the relative contribution of the core to the total radius. For higher-mass planets, the variability in the core radius fraction shows interesting trends depending on the volatile fractions. At low water fractions (up to 10–15%), the variability is largely controlled by the gas fraction, as indicated by the approximately horizontal contours. This suggests that, in this regime, changes in atmospheric content have a more significant impact on the core radius fraction. Conversely, at higher water fractions (>15%), the contours become more vertical, indicating that variations in water content dominate over the gas content in influencing the core radius fraction.

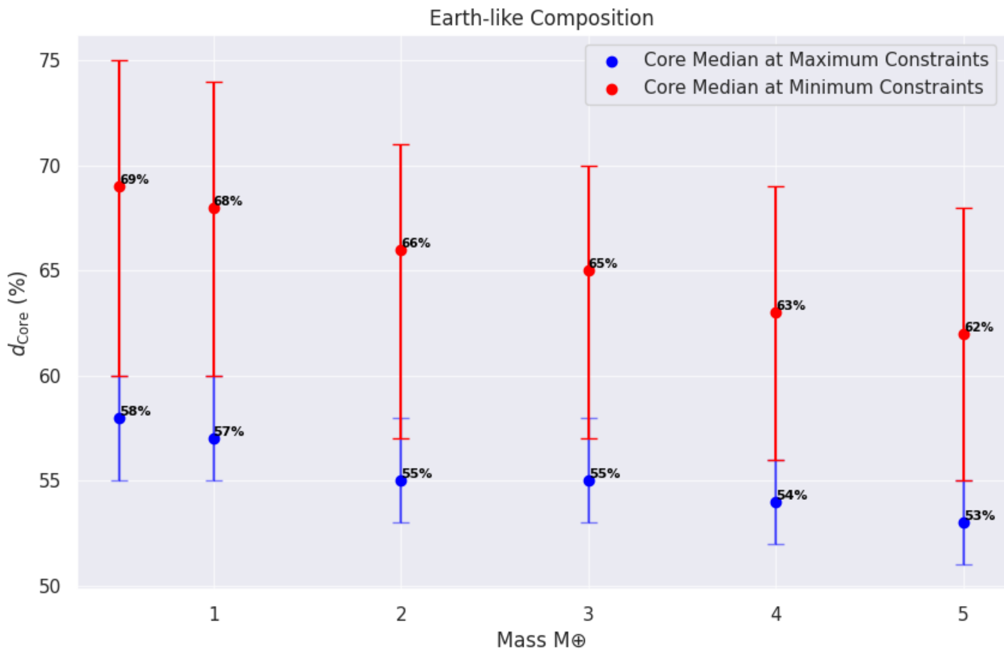

Figure 4.6: The core radius fraction vs. planetary mass plot under minimum and maximum constraints plot for planets with Earth-like composition as a function of planetary mass. The plot shows the median core radius fraction (dots) under two different constraint conditions: minimum constraints (red) and maximum constraints (blue). The error bars represent the range of core radius fraction values, spanning from the minimum to the maximum values permitted by the constraints, with the median indicating the midpoint of this distribution.

Figure 4.6 simplifies this relation by extracting the core radius fraction at both maximum and minimum constraints for water and gas from the contour plot for each planetary masses. The blue points in the plot represent the core radius fraction when the planets are subject to maximum constraints on water and gas (lower limits from contour plot), while the red points shows the median core radius fraction when minimum constraints are applied (higher limits from the contour plot). The decreasing trend of core radius fraction with increasing planetary mass is evident from both the plots illustrating that, as planets become more massive, the core contributes less to the total radius since these planets are able to accommodate larger fractions of lighter materials. This trend highlights how the internal structure of planets changes with mass and composition, particularly the core-to-total radius ratio as a function of volatile content.

4.4 Constrained Predictions for Planets with Mercury- and Moon-like Compositions

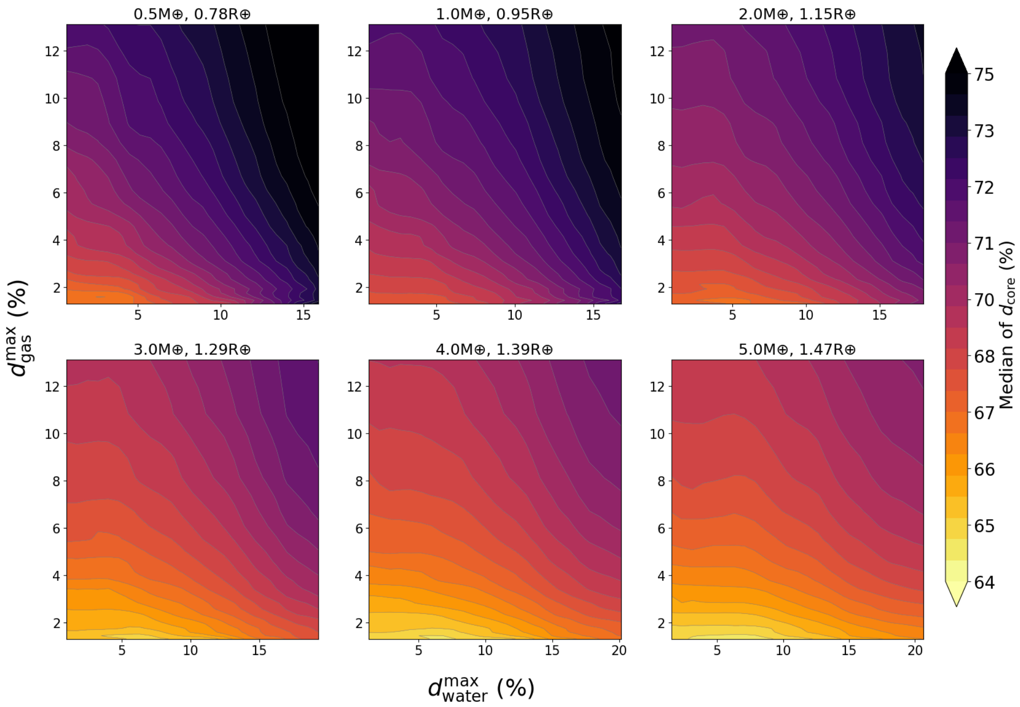

Figure 4.7: The core radius (d_{core}) fraction as a function of water and gas fractions plot for planets with Mercury-like composition with masses ranging from 0.5 to $5M_{\oplus}$. Each panel represents a different planetary mass, with the core radius fraction varying as a function of the maximum allowed water (d_{water}) and gas (d_{gas}) fractions.

We also studied the effect of constraints on different planetary compositions. For Mercury-like composition, the core radius fraction is assumed to be 70%, while for Moon-like composition, it is set at 20%. The core radius fraction as a function of water and gas fractions plot for Mercury-like composition is shown in Figure 4.7, alongside its corresponding core radius fraction vs. planetary mass plot under maximum and minimum constraints in Figure 4.8. For Moon-like composition, the respective plots are presented in Figures 4.9 and 4.10. These figures illustrate the dependence of the core radius fraction on water and gas content, as well as how it varies with planetary mass under different constraints for different compositional scenarios.

For a planet with $1M_{\oplus}$ and a Mercury-like composition, the core radius fraction is notably high. In the scenario with only minimum amount of water and gas, the core radius fraction becomes 69%, while considering the maximum amount of water and gas, it reaches 75%. As the mass increases, we can see that core radius fraction decreases slightly but remains relatively well constrained. This indicates that even with increased volatile content, the core remains dominant in planets with Mercury-like compositions. This is indicative of a planet with a large iron core, similar to what is observed for Mercury in our Solar System. In the core radius fraction vs. planetary mass plot under maximum and minimum constraints 4.8, the relatively narrow range between the constrained and unconstrained core fractions suggests that the internal structure of a planet with Mercury-like compositions at $1M_{\oplus}$ remains largely dominated by its iron-rich core, with only minor effects from water and gas content on the core size.

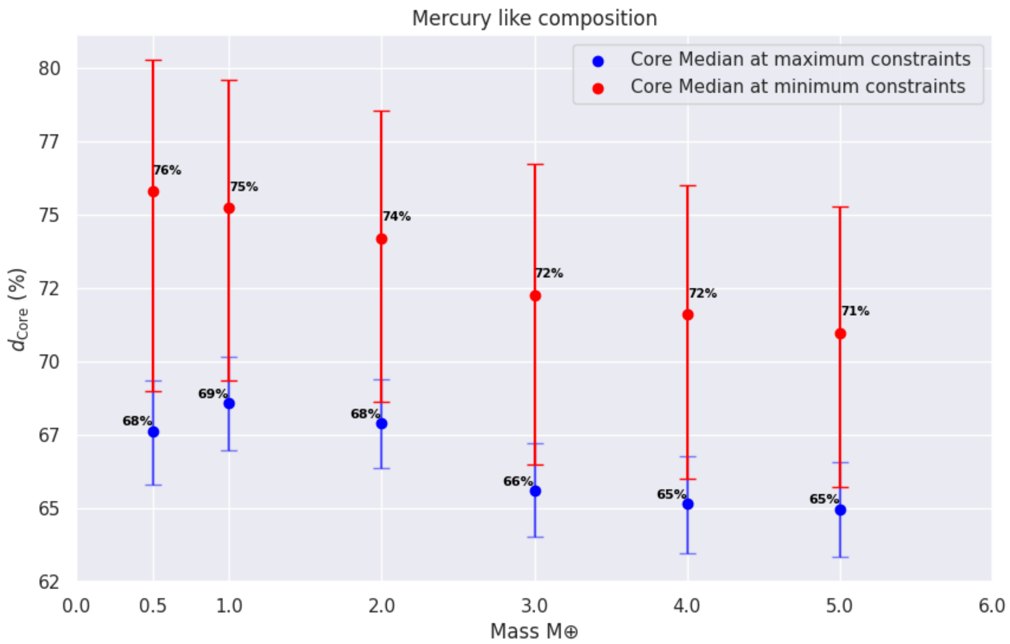

Figure 4.8: The core radius fraction vs. planetary mass plot under minimum and maximum constraints for planets with Mercury-like composition as a function of planetary mass. The plot shows the median core radius fraction (dots) under two different constraint conditions: minimum constraints (red) and maximum constraints (blue). The error bars represent the range of core radius fraction values, spanning from the minimum to the maximum values permitted by the constraints, with the median indicating the midpoint of this distribution.

By contrast, for Moon-like composition at $1M_{\oplus}$ in Figure 4.9, the core radius fraction is significantly lower and less constrained compared to the Mercury like planets of the same mass. The core radius fraction starts around 60%, but as the water and gas fractions decrease, it can drop to approximately 42% which is way off from the true value of core radius fraction of Moon which is 20%. This indicates that a Moon-like planet with $1M_{\oplus}$ is more sensitive to volatile content, and the core size can vary substantially with the presence of water and gas. The amplitude plot in Figure 4.10 shows a wide separation between the constrained and unconstrained cases, highlighting the variability in internal structure for Moon-like compositions, especially when volatile elements are present. This reflects the more silicate-rich nature of Moon-like planets, where the core is smaller.

Figures 4.11 and 4.12 compare the impact of water and gas constraints on core radius fraction across different planetary compositions. Under minimum constraints, the Moon-like planet exhibits the lowest core radius fraction among the three, deviating significantly from its expected value, while the Earth-like planet lies in between, and the Mercury-like planet maintains the highest core radius fraction, closely matching its expected structure. With maximum constraints, the relative positions of the distributions remain the same, but the Moon-like planet

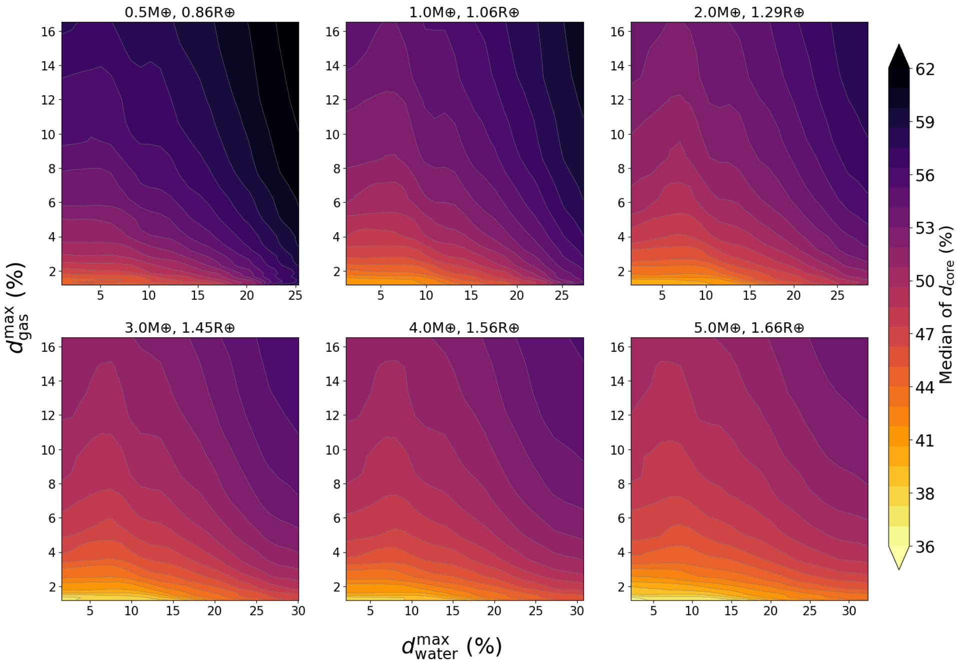

Figure 4.9: The core radius fraction (d_{core}) as a function of water and gas fractions plot for planets with Moon-like composition with masses ranging from 0.5 to $5M_{\oplus}$. Each panel represents a different planetary mass, with the core radius fraction varying as a function of the maximum allowed water (d_{water}) and gas (d_{gas}) fractions.

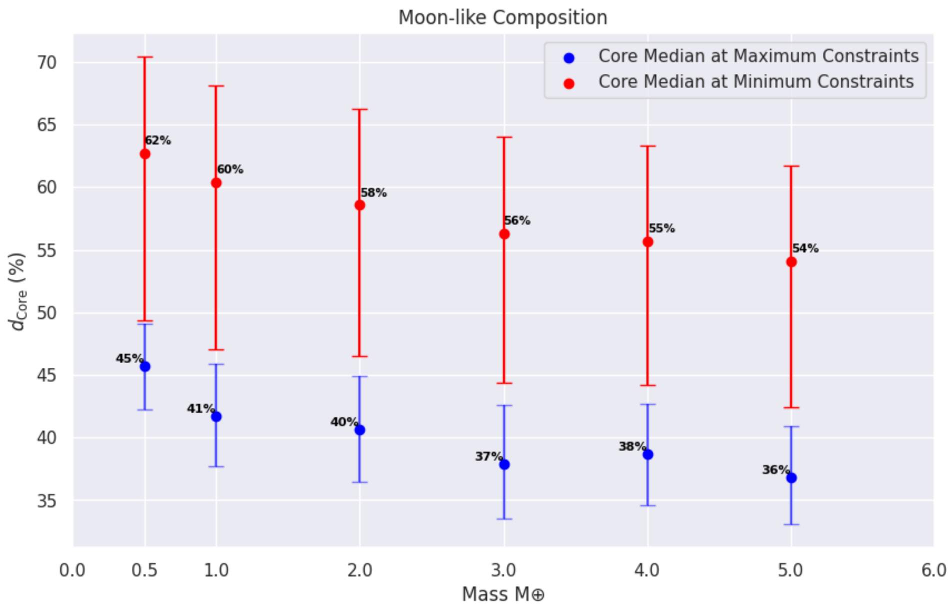

Figure 4.10: The core radius fraction vs. planetary mass plot under minimum and maximum constraints plot for planets with Moon-like composition as a function of planetary mass. The plot shows the median core radius fraction (dots) under two different constraint conditions: minimum constraints (red) and maximum constraints (blue).The error bars represent the range of core radius fraction values, spanning from the minimum to the maximum values permitted by the constraints, with the median indicating the midpoint of this distribution.

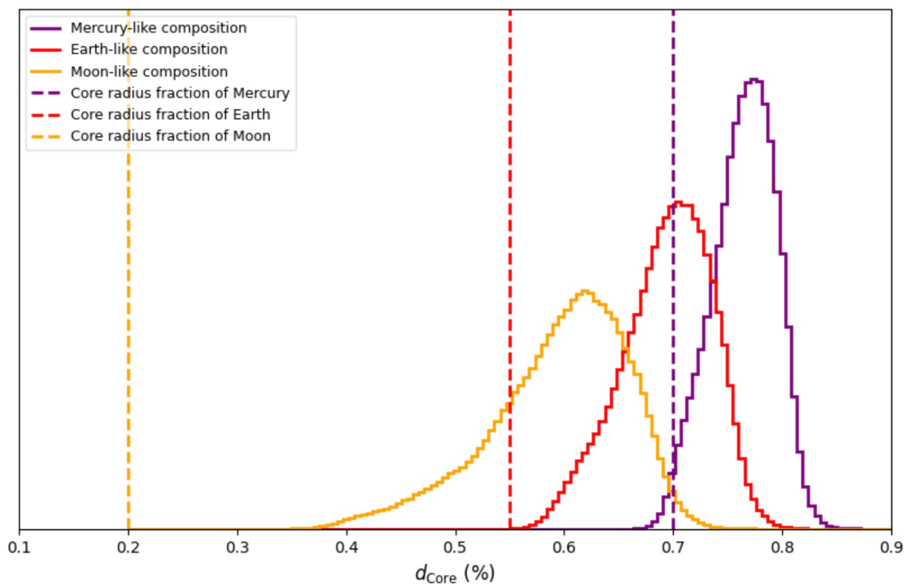

Figure 4.11: Marginal distribution of core radius fraction (d_{core}) under minimum constraints for different planetary compositions at $1M_{\oplus}$. The distributions are shown for Mercury-like, Earth-like, and Moon-like compositions, with dashed lines indicating the corresponding core radius fractions for Mercury, Earth, and Moon.

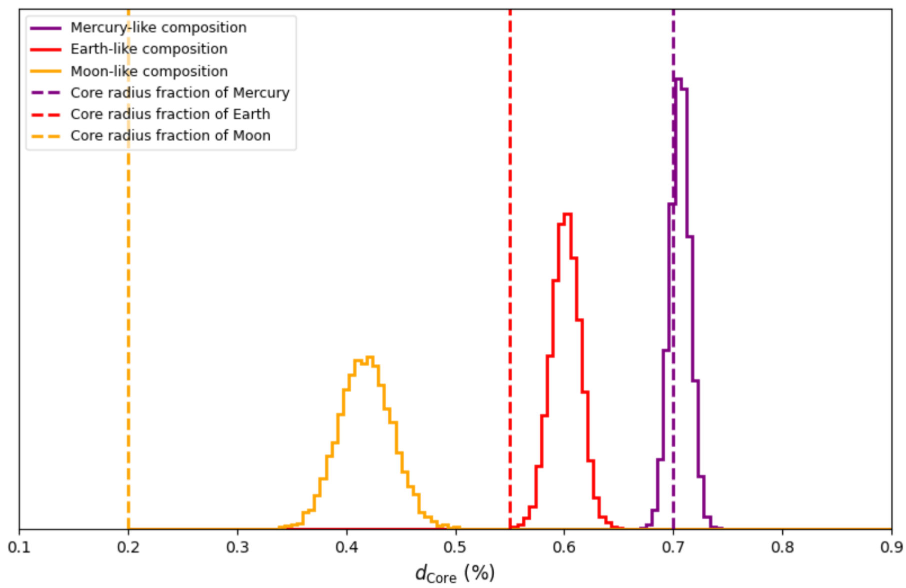

Figure 4.12: Marginal distribution of core radius fraction (d_{core}) under maximum constraints for different planetary compositions at $1M_{\oplus}$. The distributions are shown for Mercury-like, Earth-like, and Moon-like compositions, with dashed lines indicating the corresponding core radius fractions for Mercury, Earth, and Moon.

shifts closer to its expected core fraction while still being more affected than the other compositions. The Earth-like planet remains largely unchanged, while the Mercury-like planet is nearly unaffected. This comparison highlights that applying stronger constraints primarily improves the accuracy of core radius fraction estimates for compositions with lower core fractions.

4.5 Effect of Observational Uncertainties and Constraints on Interior Predictions

The upcoming exoplanet mission PLATO (Rauer et al. 2014) will significantly improve the accuracy of mass and radius measurement of planets, particularly in the low-mass regime. PLATO is expected to deliver radius accuracies of upto 3%, and with the aid from ground-based telescopes, mass accuracies to 10% or better. These observational improvements will help to better constrain the distributions of the core and also mantle radius fraction, allowing more accurate estimates of the planet's internal composition. This is especially crucial for low-mass exoplanets, given their potential habitability.

Figure 4.13 illustrates the impact of varying mass uncertainties on the internal structure of an Earth-like planet ($1 \pm \delta M\, M_{\oplus}$, $1 \pm 0.05 R_{\oplus}$, $T_{\text{eq}} = 255$ K). The different colors represent mass uncertainties ranging from 1% to 20%, while the radius uncertainty is fixed at 5%. These colors show how these uncertainties affect core radius fraction (d_{core}), mantle radius fraction (d_{mantle}), water fraction (d_{water}), and gas fraction (d_{gas}), when no constraints are placed on the allowed amount of water and gas. All the four distributions remain remarkably stable upon increasing mass uncertainty. For example, the core radius fraction (d_{core}) shows only a slight broadening as mass uncertainty increases from 1% (yellow) to 20% (dark blue). This suggests that the internal structure, particularly the core, is not highly sensitive to mass uncertainties in the 1% to 20% range. A similar behavior is observed for the mantle, water, and gas fractions, with only minor variations despite the increase in mass uncertainty.

Uncertainties in mass have minimal effect on internal structure parameters. In contrast, radius uncertainties have a much more significant impact on determining the core, mantle, water, and gas fractions, as well as their accuracies. As the planet mass scales with the cube of the radius, small changes in radius are quickly amplified and can have a strong influence on interior predictions. Therefore, addressing radius uncertainties is crucial for improving the accuracy of observational data.

The three figures 4.14a, 4.14b and 4.14c illustrate how varying radius uncertainties (from 1% to 20%) affects the internal structure of an Earth-like planet ($1 \pm 0.1 M_{\oplus}$, $1 \pm \delta R_{\oplus}$, $T_{\text{eq}} = 255$ K), under different constraints: no constraints, moderate constraints, and maximum constraints respectively. Each plot shows the distributions of core radius fraction (d_{core}), mantle radius fraction (d_{mantle}), water fraction (d_{water}), and gas fraction (d_{gas}). In Figure 4.14a, which illustrates the case with no constraints and varying radius uncertainty, the distributions for the core and mantle radius fractions exhibit well-defined peaks that remain relatively stable as radius uncertainty increases. However, the widths of these distributions broaden significantly, particularly at higher uncertainties (e.g., 10% and 20%), indicating increased variability in their values.

In Figure 4.14b, under moderate constraints on water and gas content, the distributions for the core and mantle radius fractions remain well-defined, with stable peaks as radius uncertainty increases when compared to minimum constraints case. Compared to the no-constraints

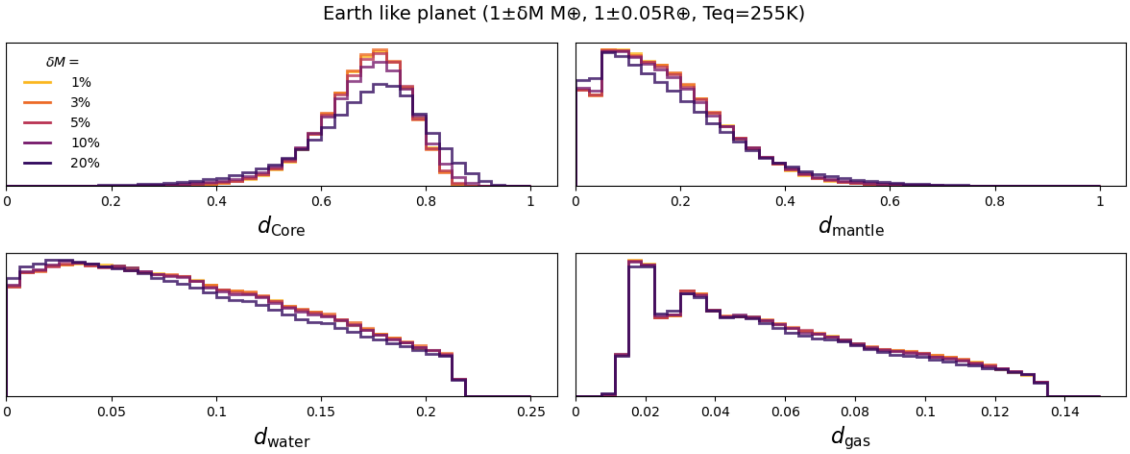

Figure 4.13: Impact of varying mass uncertainties on the internal structure of an Earth-like planet ($1 \pm \delta M\ M_{\oplus}$, $1 \pm 0.05 R_{\oplus}$, $T_{\mathrm{eq}} = 255$ K). The four subplots show the distributions of core radius fraction (d_{core}), mantle radius fraction (d_{mantle}), water fraction (d_{water}), and gas fraction (d_{gas}) under different mass uncertainties (1%, 3%, 5%, 10%, 20%). Despite increasing mass uncertainty, the internal structure remains stable, with only slight broadening of the distributions, particularly for the core radius fraction, indicating that Earth-like planets' interior structures are not highly sensitive to mass uncertainties within this range.

scenario, the broadening of these distributions is less pronounced, indicating that the imposed constraints on water and gas help reduce the variability in the core and mantle fractions. At higher levels of radius uncertainty (e.g., 10% and 20%), the distributions for both the core and mantle still show some broadening, though it is more contained than in the minimum constraints case.

In Figure 4.14c, which depicts the case with maximum constraints on water and gas content, the distributions for both core and mantle radius fractions are more sharply defined and exhibit reduced broadening as radius uncertainty increases. The core radius fraction remains stable across all levels of radius uncertainty, and the mantle radius fraction similarly shows limited variability. We also notice that ExoMDN predicts a small number of solutions at very low core radius fractions with d_{core} between 0 and 0.2 (and correspondingly high mantle radius fractions). These solutions are non-physical and should be disregarded. The exact reason why they appear is being investigated. It may be related to the limited amount of samples used to train the network when maximum constraints on water and gas are considered in combinations with large uncertainties in radius. Nevertheless, these results highlight the effectiveness of imposing strong constraints on volatile components in significantly reducing the impact of radius uncertainties on the predicted core and mantle structure. Compared to the minimum constrained and moderate-constrained cases, the core and mantle distributions here are much more compact, indicating that maximum constraints on water and gas content help to strongly constrain the internal structure of the planet.

In summary, across all the three plots illustrate how varying radius uncertainties and the level of constraints impact the distributions of core and mantle radius fractions. In the minimum constraint scenario, both core and mantle fractions exhibit broad distributions that widen

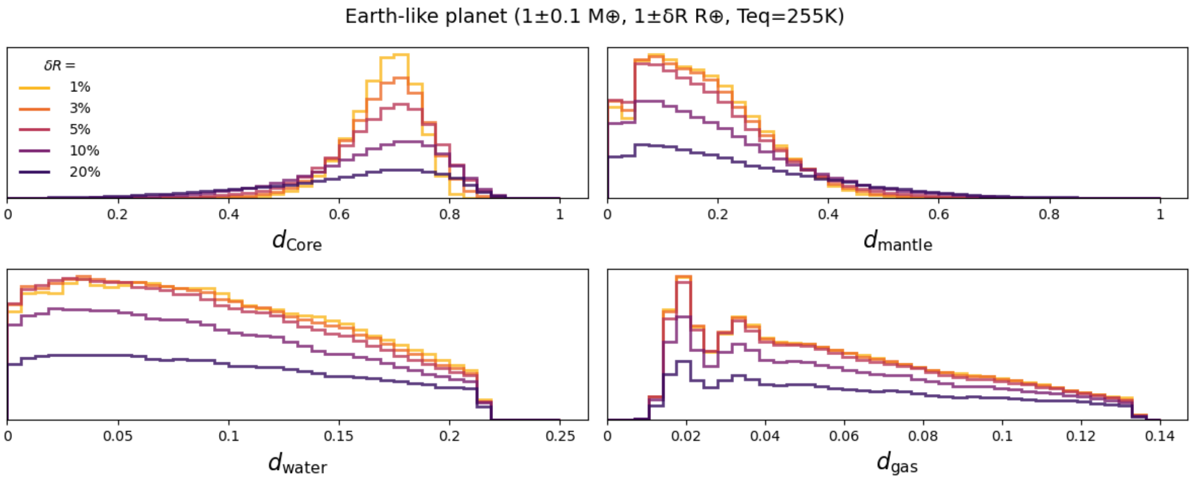

(a) Minimum constraints on water and gas along with radius uncertainty.

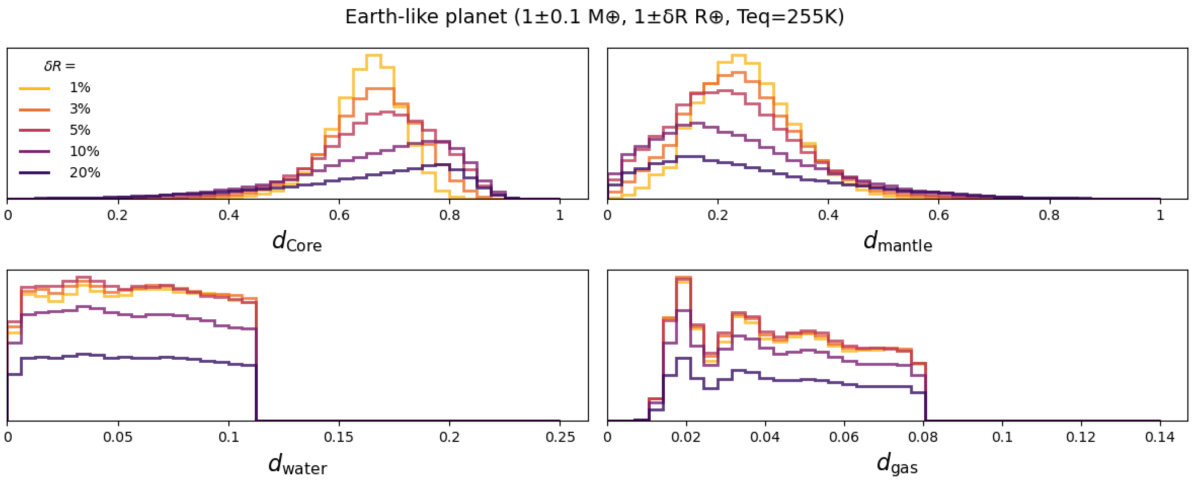

(b) Moderate constraints water and gas along with radius uncertainty.

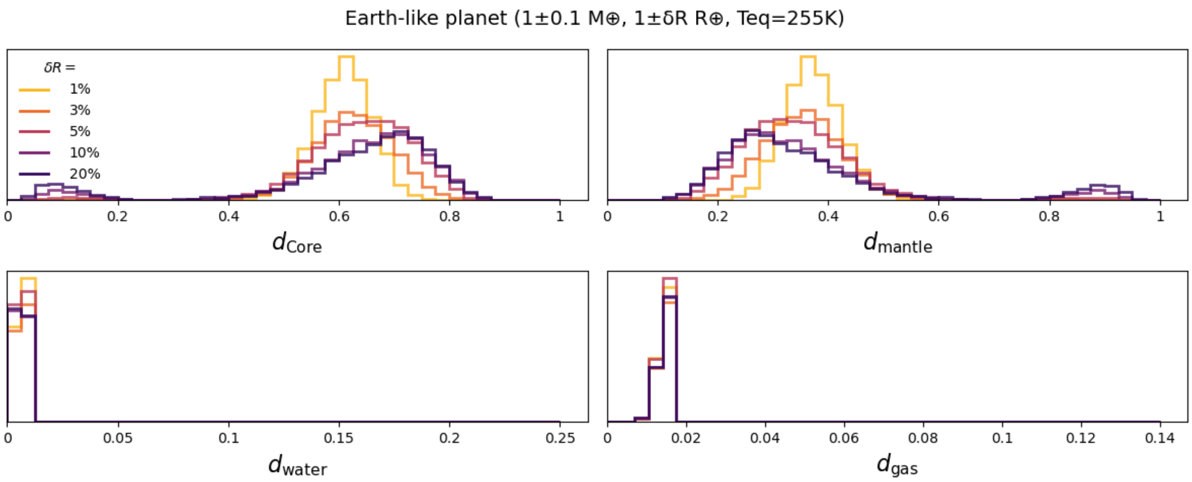

(c) Maximum constraints water and gas along with radius uncertainty.

Figure 4.14: The impact of varying radius uncertainties ($1 \pm \delta R\, R_{\oplus}$) on the internal structure of an Earth-like planet ($1 \pm 0.1\, M_{\oplus}, T_{\text{eq}} = 255\, K$), with mass uncertainty fixed at 10%. The subplots illustrate the distributions of core radius fraction (d_{core}), mantle radius fraction (d_{mantle}), water fraction (d_{water}), and gas fraction (d_{gas}) under varying radius uncertainties (1%, 3%, 5%, 10%, 20%).

significantly with increasing uncertainties. Under moderate constraints, the distributions are narrower but still show sensitivity to higher uncertainties. With maximum constraints, the distributions for both core and mantle fractions are sharply defined and exhibit minimal broadening, indicating that strong constraints effectively mitigate the impact of radius uncertainties on the internal structure predictions.

Figure 4.15 summarizes the effect of varying radius uncertainties (1%, 3%, 5%, 10%, 20%) and different constraint levels (maximum, moderate, and no constraints) on the core radius fraction (d_{core}) for an Earth-like planet. Under maximum constraints, the core radius fraction remains tightly constrained, with narrow distributions peaking around 0.6, which is close to Earth's actual core radius fraction (green dashed line). This shows that strong constraints on water and gas enable a precise determination of the core size, even with increasing uncertainties. With moderate constraints, the distributions broaden slightly, particularly for higher uncertainties (10% and 20%), but the core fraction remains relatively stable around 0.6. However, without constraints, the distributions show significant broadening as uncertainties increase, leading to greater variability in the core radius fraction. This indicates that, while constraints on volatile content reduce the impact of radius uncertainties, the lack of constraints makes it more challenging to accurately infer the core size, especially at higher uncertainty levels.

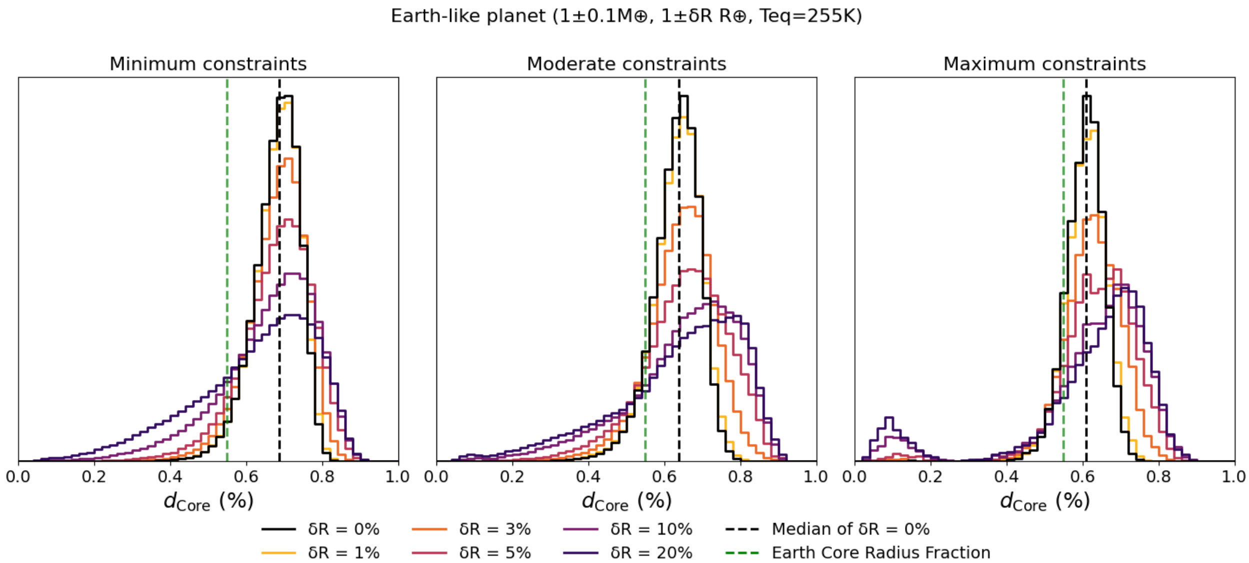

Figure 4.15: Summary plot of the impact of radius uncertainties and constraint levels on the core radius fraction (d_{core}) for an Earth-like planet ($1 \pm 0.1 M_{\oplus}, 1 \pm \delta R R_{\oplus}, T_{\text{eq}} = 255$ K). The figure illustrates the effect of varying radius uncertainties ($1\%, 3\%, 5\%, 10\%, 20\%$) under three constraint levels: no constraints (left), moderate constraints (middle), and maximum constraints (right), with mass uncertainty fixed at 10%.

4.6 Effect of Observational Uncertainties and Constraints on Interior Predictions for Different Compositions

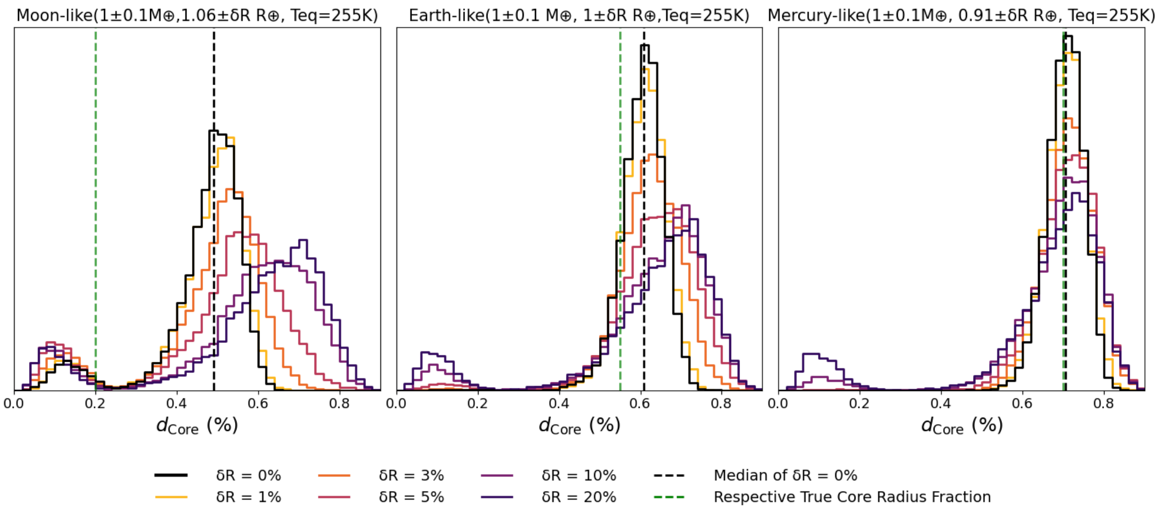

Figure 4.16: Impact of radius uncertainties on the core radius fraction (d_{core}) for planets with Moon-like, Earth-like, and Mercury-like compositions under maximum constraints. The figure illustrates the effect of varying radius uncertainties ($1\%, 3\%, 5\%, 10\%, 20\%$) on the predicted d_{core}. The dashed green line in each panel represents the true core radius fraction for the corresponding composition.

Figure 4.16 shows the impact of radius uncertainties on the predicted core radius fraction (d_{core}) for planets with Moon-like, Earth-like, and Mercury-like compositions. The vertical dashed green line in each panel represents the true core radius fraction for the corresponding composition.

For Moon-like compositions, the d_{core} distributions show significant variability, even at low radius uncertainties ($\delta R = 1\%, 3\%$). As the uncertainty increases, the distributions broaden and shift to the right, deviating from the true core radius fraction. This variability is due to the less dense interior of Moon-like planets, which allows for more flexibility in possible internal structures, resulting in greater degeneracy even under maximum compositional constraints.

For Earth-like compositions, the d_{core} distributions are more centered around the true core radius fraction, with only a modest rightward shift at lower uncertainties. As uncertainty increases, the distributions widen but remain less variable compared to the Moon-like case, reflecting the intermediate density and compositional constraints of Earth-like interiors.

In contrast, Mercury-like compositions demonstrate robust predictions of d_{core} even at the highest levels of uncertainty. The distributions remain tightly clustered around the true core radius fraction, with minimal broadening or deviation, regardless of the level of radius uncertainty. This is due to the high density and well-constrained interior of Mercury-like planets, which leaves little room for variability or degeneracy in the inferred core radius fraction.

In summary the variability in d_{core} predictions depends strongly on the planet's composition. Moon-like compositions exhibit substantial variability and degeneracy due to their less dense interiors, even under maximum constraints. In contrast, Mercury-like compositions, characterized by their dense cores, are far less affected by uncertainties in radius measurements, maintaining predictions close to the true d_{core}. This highlights the importance of interior density and compositional constraints in mitigating the impact of measurement uncertainties on inferred planetary structures.

Discussion

By converting the composition into mass fractions, we can quantify the amount of each component present in the planets. The corresponding plot, illustrating this in mass fractions, is provided in the Appendix in Figures 7.2, 7.4, 7.6 for Earth-like, Mercury-like and Moon-like composition, respectively. Table 5.1 summarizes the water and atmosphere mass fractions for the three planet types, as calculated using ExoMDN. Moon-like planets exhibit the highest water mass fractions, reaching up to 25%, followed by Earth-like planets with water mass fractions of up to 20%, and Mercury-like planets with the lowest water mass fractions, up to 12%. The atmospheric mass fraction is similar for all planet types, remaining no more than 0.1%. These values provide a quantitative framework for comparing the internal compositions of these planet types with the predictions of planet formation models. Such comparisons are crucial for understanding how initial conditions such as the composition of the protoplanetary disk and planetary accretion processes which affect the final structure and composition of planets.

Planet type	Water mass fraction (%)	Atmosphere mass fraction (%)
Earth like	Up to 20	Up to 0.1
Mercury like	Up to 12	Up to 0.1
Moon like	Up to 25	Up to 0.1

Table 5.1: Planet types and their mass fractions calculated using ExoMDN.

5.1 Constraints on Water from Planet Formation Models

Planet formation is a natural consequence of star formation, with the protoplanetary disk providing the stage for this process. This disk, which contains 1-2% of star's mass, serves as the birthplace of planetary systems, initially composed of microscopic solid materials. Protoplanetary disks, made up of gas and dust are characterized by the radial increase in temperature and pressure as one moves closer to the central star. Within these disks, there are specific radii where various volatiles condensate, known as ice lines. Among these volatiles, the water ice-line is particularly important for planetary formation.

Interactions between protoplanetary disks and forming planets are strongly influenced by the disk's structure and physical processes driving the evolution. Recent studies have shown that large volatile fractions observed in close-in exoplanets are likely the result of large-scale migration within the planetary system (e.g, Bitsch et al. 2019). To understand the constraints on water mass fraction in low-mass exoplanets, it is crucial to discuss the various mechanisms that influence how water is incorporated into these planets and ultimately determine their final mass fraction.

5.1.1 Fragmentation

Terrestrial planets form through coagulation of micrometer-sized dust grains into planetesimals, ranging from 1 to 100 km in size (Weidenschilling et al. 1997). As planetesimals grow, their velocity dispersion increases due to gravitational excitation from growing planetary embryos. These increased velocity of the planetesimals causes fragmentation during collisions. The later stages of terrestrial planets are dominated by collisional fragmentations (Alexander & Agnor 1998; Wallace et al. 2017; Clement et al. 2019) and hit-and-run collisions (Chambers 2013; Emsenhuber & Asphaug 2019; Emsenhuber et al. 2021), which influence the stability of the system, as well as the growth and composition of the planets.

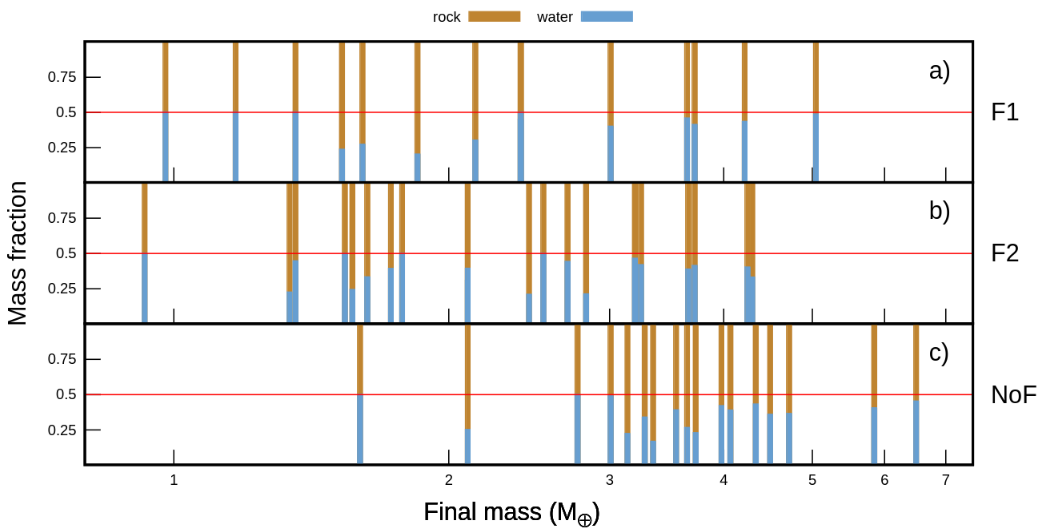

Figure 5.1: The fraction of rock and water in planets that survived in the habitable zone (HZ) after 400 Myr of evolution is shown for simulations with a higher fragmentation mass ($M_{\rm min} = 0.018\,M_\oplus$, F1), a lower fragmentation mass ($M_{\rm min} = 0.0018\,M_\oplus$, F2), and no fragmentation (NoF). Here, $M_{\rm min}$ represents the minimum individual mass assigned to fragments during the simulations. Dark yellow bars represent rocky content, dark blue bars represent water content, and the red line indicates the initial water fraction at the start of the simulation (from Dugaro et al. (2020)).

Dugaro et al. (2020) studied the rock and water fractions in planets within the habitable zone, showing how they are influenced by different fragmentation masses and is illustrated in Figure 5.1. In a related work, Burger et al. (2020) explored water delivery to terrestrial planets during the late stages of formation, considering various collision scenarios beyond just perfect mergers. They found that fewer, more significant collisions with embryo-sized or larger bodies deliver most of the planet's final water inventory. While water loss in individual collisions are relatively low, cumulative effects of multiple collisions can lead to substantial water depletion. Their study also suggests that most potentially habitable planets initially accrete dry material and only receive significant water delivery after reaching a to at least 50% and often to over 90% of their final mass. The range of water content in terrestrial planets within the habitable zone can vary widely due to collision dynamics, with water inventories often being reduced by a factor of two or more compared to scenarios that assume perfect merging.

5.1.2 Migration

Gravitational interactions between a planet and the surrounding gas in a protoplanetary disk create tidal torques that can cause a planet to shift inward or outward over time in a process known as planetary migration. Low-mass planets (with mass less than that of Neptune) lack gravitational strength to significantly alter the disk and undergo what is called Type-I migration. Earlier models (Goldreich & Tremaine 1980; Ward 1997) only considered Lindblad torques (**?**), which are typically negative, leading to fast inward migration. However, recent models (Paardekooper & Mellema 2006; Kley et al. 2009; Lega et al. 2015) have introduced the concept of horseshoe drag, where the net torque on low-mass planets can be negative, zero or positive. This means that planet can continue moving inward, stop and remain in place, or move outward respectively.

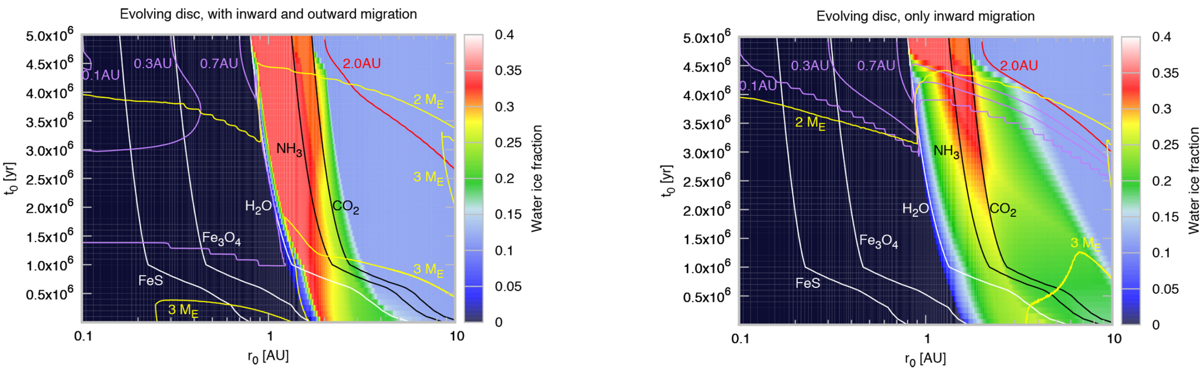

Figure 5.2: Impact of planetary migration and the evolving ice-line on the water ice fraction. Outward migration allows planets to retain high water content, while inward migration reduces it. This interplay creates a gradient in water content, highlighting the complex processes shaping planetary compositions and structures. The x-axis represents the distance r_0 from the star, the y-axis indicates the evolution over time t_0 , and the color gradient represents the water ice fraction of the planets (from Bitsch et al. (2019)).

Bitsch et al. (2019) studied the water content of super-Earths ranging from $0.01\ M_\oplus$ to $10\ M_\oplus$ by examining the interplay between pebble accretion, planet migration, and disc evolution using 2D hydrodynamical simulations, as shown in Figure 5.2. The study tracked the accretion of major solid and ice-forming species to determine the final composition and the final water mass fraction of close-in super-Earths. The findings revealed that planets forming outside the water-ice line (~ 5.5 AU) without significant migration during their lifetime can retain up to $\sim 35\%$ water ice by mass, while those forming closer to the star are primarily rocky in composition. Inward migration significantly affects the water content, as planets initially accrete water-rich material but lose much of it upon crossing the ice line. This results in gradient in water content, with most planets ending up with mass less than they started with. The evolution of the ice-line further diversifies water fractions, with planets swept by the ice-line later in their growth phase having lower water content. Outward migration, on the other hand, allows planets to retain high water content ($\sim 35\%$). Planets containing up-to $\sim 25\%$ of water by mass are typically those that form beyond the water ice-line and migrated inward, accreting both rocky and icy materials. The exact water content depends on the dynamics of protoplanetary disk, the migration path, and the timing of formation relative to the evolving ice-line.

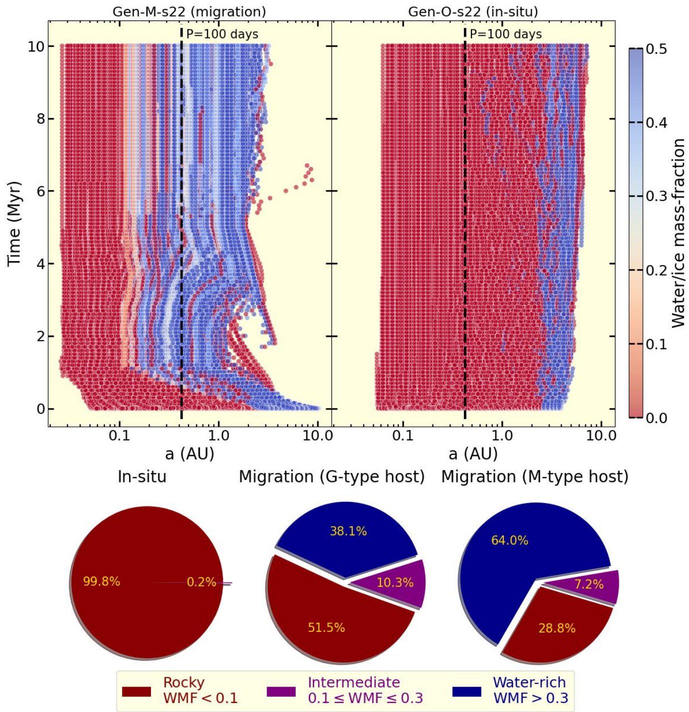

Figure 5.3: Top panel: Water mass-fractions of planetary embryos from migration (left) and in-situ (right) simulations, based on Genesis database, showing their evolution over the course of simulations assuming a G-type host star. Bottom panel: Distributions of water mass-fraction (WMF) of the cores produced by all the migration models combined and the in-situ models (from Chakrabarty & Mulders (2024)).

Planetary migration significantly impacts the composition of the planets. Since the outer regions of the disk, beyond the water ice line, are richer in volatiles due to lower temperatures, planets that migrate inward toward the HZ are likely to be more volatile-rich than those formed in situ. Planets forming beyond the water-ice tend to accrete large amounts of water, comprising approximately 30-40% of their total solid mass (Thiabaud et al. 2015). Chakrabarty & Mulders (2024) provided a comprehensive analysis of formation and evolution of water-rich exoplanets employing different migration scenarios. Their study focused on how atmospheric loss could influence planets formed through both migration and in-situ processes. They suggested that even after atmospheric loss, most planets around G-type stars, particularly those that formed beyond the water ice-line, can retain their water content at 1 AU is given in the Figure 5.3. This diverse formation scenarios can explain various planetary compositions, particularly for those with significant water content.

Results of my model suggests that, Earth-like planets with masses ranging from 0.5 to $5M_\oplus$ could contain nearly up-to 20% water by mass. Mercury-like planets, characterized by a large core radius fraction (approximately 70%), exhibit a reduced water content, with maximum around 12%. Conversely, Moon-like compositions have a higher capacity for water retention, with mass fractions up to 25%. These specific water content values for Earth-like, Mercury-like, and Moon-like planets in our model are consistent with the variations in planetary formation and composition observed in the simulations. This consistency supports the hypothesis that different formation scenarios can lead to substantial water retention, thereby reinforcing the insights derived from these N-body simulations.

5.2 Constraints from Atmosphere Loss Models

During early stages of planetary formation, once a core has formed, low-mass planets can begin to accrete gas from their protoplanetary disk, although in lesser amount compared to gas giants (Lee & Chiang 2016; Ginzburg et al. 2016). This gas, predominantly composed of hydrogen and helium, forms what is known as the primary atmosphere. The amount of gas accreted by a planet depends on the density of the surrounding disk and timescale over which the gas remains available. The retention of this gas is influenced by the planet's gravity, temperature, and the stellar radiation it receives.

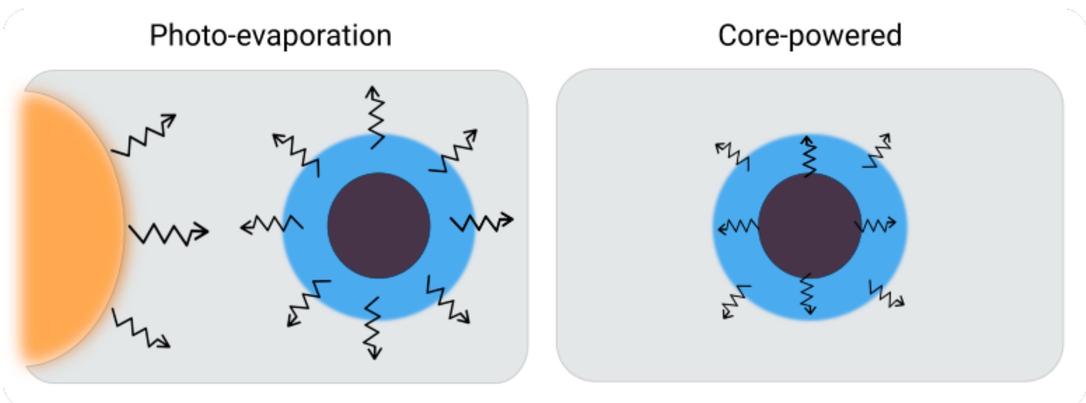

Figure 5.4: Schematic representation of atmospheric loss mechanisms in exoplanets. The left panel illustrates photoevaporation, where high-energy radiation from the host star drives atmospheric escape. The right panel shows core-powered mass loss, where the planet's own internal heat contributes to atmospheric escape.

Atmospheric escape processes are critical in shaping the evolution of a planet's atmosphere and its final composition. These processes, illustrated in Figure 5.4, involve mechanisms like hydrodynamic escape driven by UV stellar radiation, can deplete this gas, particularly in planets that orbit close to their host stars. However, super-Earths with their substantial gravity, can retain some of this atmosphere over long term (Lammer et al. 2014). Additionally, a planet's own luminosity can also favor atmosphere loss. In this section, we will explore atmospheric loss processes and discuss how these can influence the final composition of planets.

5.2.1 Photo-Evaporation

Planets orbiting close to their host star are exposed to high-energy radiation, which can contribute a significant fraction of the energy to overcome their gravitational binding energy (Lammer et al. 2003; Davis & Wheatley 2009), which can lead to significant atmosphere loss particularly for planets with substantial gaseous envelope (Owen & Jackson 2012). As a result, planets that lose their gaseous envelopes become smaller in size and higher in density compared to planets located farther from their host stars, which are less affected by atmospheric escape (Lopez et al. 2012; Lopez & Fortney 2014; Owen & Wu 2013). This evaporation theory also predicts the existence of an "evaporation valley" or "radius valley" (discussed in Section 2.2, which refers to a range of planetary radii where planets are either completely stripped of their envelopes or retain a substantial portion of them (Owen & Wu 2013; Lopez & Fortney 2013).

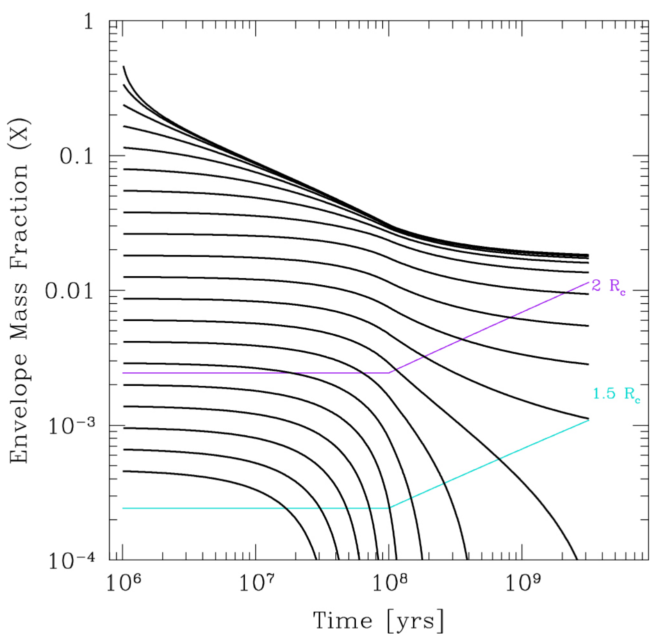

Figure 5.5: Loss of atmosphere as function of time, for planet models with a range of initial envelopes (from Owen & Wu (2017)).

Owen & Wu (2017) found that the high-energy flux from host stars, particularly in the first 100 million years of the evolution, drives the process of photoevaporation. Figure 5.5 illustrates that nearly all atmospheric erosion occurs within this first 100 million years where the host star emits high-intensity XUV radiation. Planets with low initial envelope masses (less than a few percent) are entirely stripped of their atmospheres in this time-frame. In contrast, planets with higher initial envelope masses (around 10% or more) lose a significant portion of their envelopes but stabilize at an envelope mass fraction of approximately 1%. After this initial phase of rapid erosion, the rate of mass loss decreases, leading to a stable envelope mass. This patterns supports the hypothesis that photoevaporation is most effective in the early stages of a planet's life, shaping the observed distribution of planet radii and contributing to the formation of the evaporation valley.

5.2.2 Core-Powered Mass Loss

Ginzburg et al. (2018) and Gupta & Schlichting (2019) demonstrated that core-powered mass loss could also explain the presence of the radius valley, even in the absence of photoevaporation. The planetary core retains significant thermal energy from its formation. As the planet cools over time, the cooling luminosity can be comparable to, or even exceed, the gravitational binding energy of its atmosphere, leading to the complete erosion of light envelopes while preserving the heavier ones (Ginzburg et al. 2016, 2018). They also found that the effectiveness of atmospheric loss depends on the ratio of the envelope's heat capacity to that of their rocky core. Atmospheres with mass fractions of 10^{-1} and 10^{-5} are particularly vulnerable to complete loss due to the cooling luminosity of the core. Ginzburg et al. (2018) studied the evolution of 1000 planets with rocky cores of masses a few times that of Earth over a period of 3 Gyr, following the dispersion of the protoplanetary disc. Their study focused on understanding the core luminosity dependence of atmospheric mass loss in low-mass exoplanets, which creates the bimodal distribution, particularly in explaining the low densities observed in some super-Earths (Lopez et al. 2012; Lissauer et al. 2013), as shown in Figure 5.6.

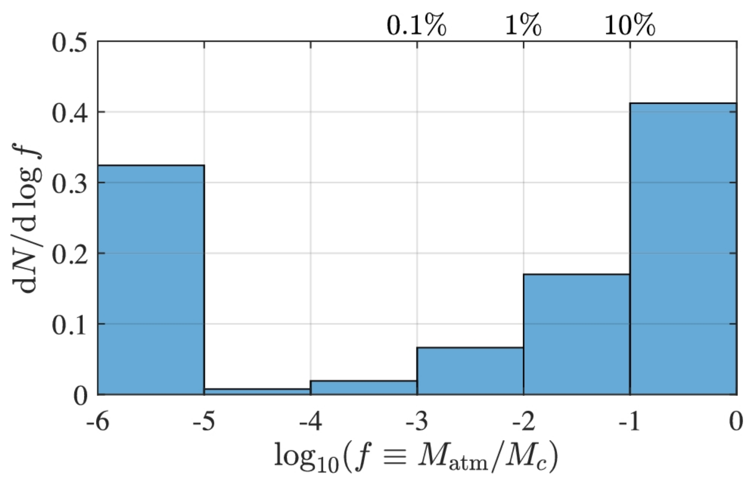

Figure 5.6: The x-axis represents the atmosphere mass fraction and y-axis shows the normalized number of planets, highlighting two peaks: one near $f < 10^{-6}$ for planets that have nearly lost their atmospheres, and another for planets that have retained significant atmospheres (from Ginzburg et al. (2018)).

Gupta & Schlichting (2019, 2020) extended this analysis, showing that core-powered mass loss in combination with stellar irradiation shapes the radius distribution of low-mass exoplanets over timescales ranging from few million to 100 million years. Owen & Schlichting (2023) found that core-powered mass loss dominates for lower gravity planets with higher equilibrium temperature, and photoevaporation dominates for higher gravity planets with lower equilibrium temperature.

5.2.3 Giant Impacts

Kegerreis et al. (2020) developed a scaling law to predict atmospheric loss due to planetary collisions on to terrestrial planets with relatively thin atmospheres (about 1% of the target mass). They also discussed how slow impacts can transfer gas to the target planet by displacing atmospheric gas outward, which remains gravitationally bound and eventually falls-back, while Moon-sized impacts while Moon-sized impacts on broadly terrestrial planets of masses ranging from roughly three times the Earth's mass down to few percent of its mass and with relatively thin (1%) atmospheres can strip away 10-60% of a planet's initial atmosphere. Additionally, giant impacts can alter the chemistry of the terrestrial planet's atmosphere (Lupu et al. 2014). Planets that complete their formation after the gas disk has dissipated are at greater risk of having their atmosphere stripped by giant impacts, regardless of their distance from the host star (Chance et al. 2022). The presence of an ocean can significantly increase the atmosphere compared to planets without oceans since water can facilitate more efficient kinetic energy transfer to the atmosphere, increasing the likelihood of atmospheric escape (Lock & Stewart 2023).

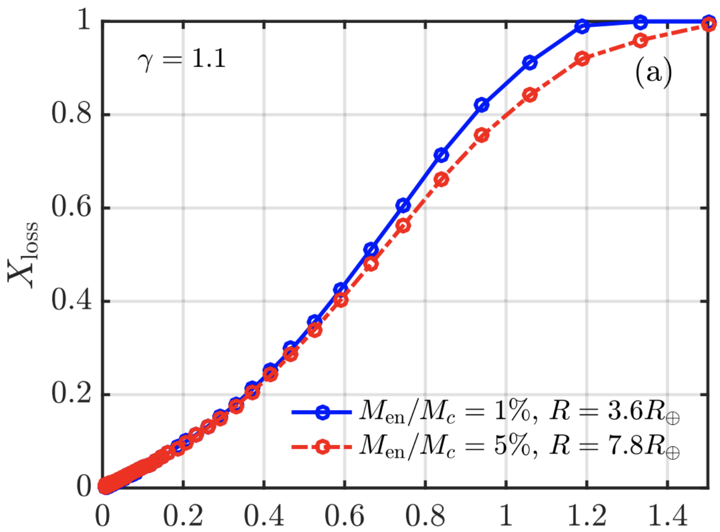

Figure 5.7: Atmosphere loss during giant impact as a function of impactor's momentum (x-axis) where it is the ratio between impactor's momentum and planet mass and fraction of envelope lost (y-axis). The two curves compare gas loss for planets with initial envelope mass fraction of 1% (blue) and 5% (red). For planets with thinner atmosphere, higher impact momentum results in greater atmospheric loss (from Inamdar & Schlichting (2016)).

Inamdar & Schlichting (2016) showed that shock-waves generated during the giant impact can propagate through the atmosphere, leading to substantial loss of gaseous envelope in low-mass exoplanets given in Figure 5.7. Furthermore, giant impact can also result in rapid mass loss due to thermal expansion of the hydrogen/helium envelope (Biersteker & Schlichting 2019).

From these studies, it is evident that planets with atmospheric mass fractions of up to $\sim 0.1\%$ are particularly susceptible to significant atmospheric loss through various mechanisms. In my models, the maximum atmospheric mass fraction can be 0.1%, which places Earth-like, Mercury-like, and Moon-like planets within this vulnerable range. This suggests that these planets are likely to experience substantial atmospheric erosion, emphasizing the critical importance of accounting for this threshold in modeling atmospheric evolution.

Summary and Outlook

6.1 Key Findings

In this thesis, we investigated the internal structure of low-mass exoplanets, focusing on how varying constraints on the water and gas content impact the distribution of different interior layers, particularly the core radius (and mass) fraction. Low-mass exoplanets are often considered to have little to no volatile content, making our study relevant for such planets. In view of upcoming missions such as PLATO, we also explored the effects of observational uncertainties in mass and radius on the prediction of internal structures. By employing an advanced machine learning model like ExoMDN trained with radial interior structure models obtained with TATOOINE, we analyzed planets with different compositions, including Earth-like, Moon-like and Mercury-like planets. The study also highlights the importance of constraints from planetary formation models and atmosphere loss mechanisms, where the age of the system plays a key role in determining the volatile content. This introduces additional constraints on water and gas, helping to refine the predictions of interior structures. This study provides new insights into the degeneracy of exoplanet interiors and offers a novel approach to mitigating this degeneracy by constraining water and gas fractions. Below, we summarize the key findings of our research:

- **Effect of Constraints on Earth-like Planets**: Constraining water and gas fractions significantly improves the accuracy of determining the core radius fraction in low-mass exoplanets. In particular, lower volatile content results in better-constrained core radius estimates, as the influence of water and gas on the planet's radius becomes minimal. High constraints on both water and gas, defined as limiting the maximum mass fractions of water ($w_{\text{water}}^{\text{max}}$) and gas ($w_{\text{gas}}^{\text{max}}$) to the upper bounds of their possible ranges—i.e., the maximum amounts of water and gas a planet could have according to the ExoMDN model—allowed us to estimate the core radius fraction with less than 5% error. This closely matches the structure of Earth-like planets, where volatiles are minimal, and the internal composition is dominated by the core and mantle.
- **Effect of Constraints on Planets with Different Compositions:** The impact of constraints varies across planetary compositions. For Mercury-like composition, I find that despite the presence of water and gas, the core radius fraction remains largely constrained. In contrast, Moon-like planets exhibit much greater variability in core radius

fraction, even under the most constrained water and gas scenarios. Additionally, I analyzed the behaviour of the core radius fraction upon increasing the planetary mass. For Moon-like planets, the core radius fraction decreases from approximately 45% at 0.5 $M_\oplus$ to around 36% at 5 $M_\oplus$. For Mercury-like planets, it decreases slightly from about 68% at 0.5 $M_\oplus$ to 65% at 5 $M_\oplus$, while for Earth-like planets, the core radius fraction decreases from approximately 58% to 53% over the same mass range. This trend highlights the importance of planetary composition and mass in determining how effectively constraints can be applied to core radius fraction estimates.

- **Effect of Constraints and Uncertainties:** Incorporating observational uncertainties is critical for estimating the interior structures. We found that uncertainties in mass have minimal impact on internal parameters, while uncertainties in the radius played a more significant role. For Moon-like compositions, the distribution peaks at 0.5 with 1% radius uncertainty and extends to 0.7 at 20% uncertainty, far from the true value of 0.2, while for Mercury-like compositions, the true value of 0.7 remains well-constrained at 1% uncertainty, shifting slightly below 0.8 at higher uncertainties. This behaviour can be attributed to Mercury's large core radius fraction (70%), which results in a well-constrained core even with small amounts of water and gas. On the other hand, the low mean density of Moon-like planets gives more room to accommodate light materials such as water and gas, leading to weaker constraints on the core radius fraction, even when volatiles are limited.

- **Constraints based on Atmospheric Escape Mechanisms and Formation Models:** The study emphasizes the importance of considering gas escape mechanisms and planetary formation models when constraining water and gas content. The age of the planetary system plays a critical role in determining the volatile composition, as older planets may have lost significant amounts of gas through atmospheric escape processes. By leveraging these insights, the constraints on water and gas content can be tailored to reflect realistic evolutionary scenarios, enabling more accurate predictions of the interior structures of low-mass exoplanets.

6.2 Limitations

Constraining water and gas enable us to understand their effects on core radius fraction. However, there are certain limitations to our model. Due to the construction of the training set, our model does not consider interior structures with completely negligible atmospheres and water. For many low-mass exoplanets with minimal or no volatiles this will gives us more closer solutions to planet's true interior structure which can be really useful for rocky planets that may have lost their atmosphere or never accumulated significant volatiles.

The current treatment of the atmosphere in the model relies on a strongly simplified isothermal approximation at the equilibrium temperature. While this approach provides a first-order estimate, it fails to capture the complexity of real planetary atmospheres, which typically exhibit both radiative and convective heat transport. These improvements would not only provide more realistic temperature and pressure profiles but can also have a significant impact on the planet's total radius and the distribution of interior layers. Future models should incorporate both radiative and convective layers to better understand the feedback between the atmosphere and the planet's interior. Also, atmospheric observations will require coupling interior models with sophisticated atmosphere models to account for the impact of atmospheric layers on planetary radius and thermal structure. Simple isothermal models are insufficient for capturing the complex interactions between the atmosphere and interior.

6.3 Further Constraints

Further constraints could include parameters like the fluid Love number k2, which provides insight into the planet's radial density distribution (Baumeister et al. 2020; Hellard et al. 2019; Kellermann et al. 2018; Padovan et al. 2018). Although k2 is challenging to measure, especially for small planets, it could serve as a valuable constraint for refining interior models if data becomes available. Additionally, stellar composition can be used as a proxy for the planet's interior composition, as planets tend to form from the same material as their host stars (Spaargaren et al. 2020; Santos et al. 2017; Dorn et al. 2016, 2015). By linking stellar metallicity and element ratios to the planet's core and mantle composition, we can further constrain the possible range of interior structures for exoplanets.

6.4 Future Directions

The inferred distributions of core, mantle, water, and gas layers significantly affect the evolution of planetary interiors, influencing heat transfer, magnetic field generation, and geological activity. Investigating how these distributions evolve over time will provide valuable insights into a planet's thermal history and atmospheric retention. Moreover, the formation of secondary atmospheres through outgassing is vital for understanding atmospheric development in low-mass rocky exoplanets. Water plays a key role in geological processes like mantle convection and plate tectonics. Future work should focus on how outgassing and water shape secondary atmospheres and influence the long-term atmospheric stability and composition of exoplanets.

Bibliography

Agarwal, S., Tosi, N., Breuer, D., et al. 2020, Geophysical Journal International, 222, 1656–1670, doi: 10.1093/gji/ggaa234

Agol, E., & Fabrycky, D. C. 2018, Transit-Timing and Duration Variations for the Discovery and Characterization of Exoplanets (Springer International Publishing), 797–816, doi: 10.1007/978-3-319-55333-7_7

Alessi, M., Inglis, J., & Pudritz, R. E. 2020, Monthly Notices of the Royal Astronomical Society, 497, 4814â4833, doi: 10.1093/mnras/staa2087

Alexander, S., & Agnor, C. 1998, Icarus, 132, 113, doi: https://doi.org/10.1006/icar.1998.5905

Alibert, Y., & Venturini, J. 2019, Astronomy and Astrophysics, 626, A21, doi: 10.1051/0004-6361/201834942

Armstrong, D. J., Gamper, J., & Damoulas, T. 2020, Monthly Notices of the Royal Astronomical Society, 504, 5327–5344, doi: 10.1093/mnras/staa2498

Azevedo Silva, T., Demangeon, O. D. S., Barros, S. C. C., et al. 2022, Astronomy amp; Astrophysics, 657, A68, doi: 10.1051/0004-6361/202141520

Baumeister, P. 2023, PhD thesis, Technische Universität Berlin, Berlin

Baumeister, P., Padovan, S., Tosi, N., et al. 2020, The Astrophysical Journal, 889, 42, doi: 10.3847/1538-4357/ab5d32

Baumeister, P., & Tosi, N. 2023, Astronomy and Astrophysics, 676, A106, doi: 10.1051/0004-6361/202346216

Beichman, C. A., & Deming, D. 2018, Observing Exoplanets with the Spitzer Space Telescope (Springer International Publishing), 1179–1203, doi: 10.1007/978-3-319-55333-7_78

Biersteker, J. B., & Schlichting, H. E. 2019, Monthly Notices of the Royal Astronomical Society, 485, 4454–4463, doi: 10.1093/mnras/stz738

Bishop, C. M. 1994, Mixture Density Networks, Technical report, Aston University, Birmingham

Bitsch, B., & Johansen, A. 2016, Astronomy and Astrophysics, 590, A101, doi: 10.1051/0004-6361/201527676

Bitsch, B., Raymond, S. N., & Izidoro, A. 2019, Astronomy and Astrophysics, 624, A109, doi: 10.1051/0004-6361/201935007

Bitsch, Bertram, Izidoro, Andre, Johansen, Anders, et al. 2019a, AA, 623, A88, doi: 10.1051/0004-6361/201834489

Bitsch, Bertram, Raymond, Sean N., & Izidoro, Andre. 2019b, AA, 624, A109, doi: 10.1051/0004-6361/201935007

Bond, I. A., Udalski, A., Jaroszyski, M., et al. 2004, The Astrophysical Journal, 606, L155–L158, doi: 10.1086/420928

Bond, J. C., O'Brien, D. P., & Lauretta, D. S. 2010, The Astrophysical Journal, 715, 1050–1070, doi: 10.1088/0004-637x/715/2/1050

Borucki, W. J., Koch, D., Basri, G., et al. 2010, Science, 327, 977–980, doi: 10.1126/science.1185402

Borucki, W. J., Koch, D. G., Basri, G., et al. 2011, , 728, 117, doi: 10.1088/0004-637X/728/2/117

Bouchet, J., Mazevet, S., Morard, G., Guyot, F., & Musella, R. 2013, Physical Review B, 87, doi: 10.1103/physrevb.87.094102

Brent, R. P. 1972, Algorithms for Minimization without Derivatives, Prentice-Hall Series in Automatic Computation (Englewood Cliffs, N.J.: Prentice-Hall)

Brown, H. 1950, Astrophysical Journal, vol. 111, p. 641, 111, 641

Buchhave, L. A., & Latham, D. W. 2015, The Astrophysical Journal, 808, 187, doi: 10.1088/0004-637X/808/2/187

Burger, C., Bazsó, , & Schäfer, C. M. 2020, Astronomy and Astrophysics, 634, A76, doi: 10.1051/0004-6361/201936366

Burn, R., Bali, K., Dorn, C., Luque, R., & Grimm, S. L. 2024. https://arxiv.org/abs/2411.16879

Carter, J. A., Agol, E., Chaplin, W. J., et al. 2012, Science, 337, 556â559, doi: 10.1126/science.1223269

Chakrabarty, A., & Mulders, G. D. 2024, Where are the Water Worlds? Identifying the Exo-water-worlds Using Models of Planet Formation and Atmospheric Evolution. https://arxiv.org/abs/2310.03593

Chambers, J. 2013, Icarus, 224, 43, doi: https://doi.org/10.1016/j.icarus.2013.02.015

Chance, Q., Ballard, S., & Stassun, K. 2022, The Astrophysical Journal, 937, 39, doi: 10.3847/1538-4357/ac8a97

Charbonneau, D., Brown, T. M., Latham, D. W., & Mayor, M. 2000, The Astrophysical Journal, 529, L45–L48, doi: 10.1086/312457

Chatterjee, S., & Tan, J. C. 2014, The Astrophysical Journal, 798, L32, doi: 10.1088/2041-8205/798/2/132

Chaushev, A., Raynard, L., Goad, M. R., et al. 2019, Monthly Notices of the Royal Astronomical Society, 488, 5232–5250, doi: 10.1093/mnras/stz2058

Chiang, E., & Laughlin, G. 2013, Monthly Notices of the Royal Astronomical Society, 431, 3444â3455, doi: 10.1093/mnras/stt424

Chiang, E., & Laughlin, G. 2013, , 431, 3444, doi: 10.1093/mnras/stt424

Clement, M. S., Kaib, N. A., & Chambers, J. E. 2019, The Astronomical Journal, 157, 208, doi: 10.3847/1538-3881/ab164f

Csizmadia, S., Hellard, H., & Smith, A. M. S. 2019, Astronomy and Astrophysics, 623, A45, doi: 10.1051/0004-6361/201834376

Davis, T. A., & Wheatley, P. J. 2009, Monthly Notices of the Royal Astronomical Society, 396, 1012–1017, doi: 10.1111/j.1365-2966.2009.14763.x

Deeg, H. J., & Alonso, R. 2018, Transit Photometry as an Exoplanet Discovery Method (Springer International Publishing), 633–657, doi: 10.1007/978-3-319-55333-7_117

Deleuil, M., Aigrain, S., Moutou, C., et al. 2018, Astronomy and Astrophysics, 619, A97, doi: 10.1051/0004-6361/201731068

Dole, S. H. 1964, Habitable Planets for Man, Blaisdell Book on the Pure and Applied Sciences (New York: Blaisdell Publishing Company)

Dorn, C., Hinkel, N. R., & Venturini, J. 2016, Astronomy and Astrophysics, 597, A38, doi: 10.1051/0004-6361/201628749

Dorn, C., Khan, A., Heng, K., et al. 2015, Astronomy and Astrophysics, 577, A83, doi: 10.1051/0004-6361/201424915

Dorn, C., Venturini, J., Khan, A., et al. 2017, Astronomy Astrophysics, 597, A37, doi: 10.1051/0004-6361/201628708

Dugaro, A., de El'ia, G. C., & Darriba, L. A. 2020, Astronomy & Astrophysics. https://api.semanticscholar.org/CorpusID:221090541

Einstein, A. 1936, Science, 84, 506–507, doi: 10.1126/science.84.2188.506

Emsenhuber, A., & Asphaug, E. 2019, The Astrophysical Journal, 875, 95, doi: 10.3847/1538-4357/ab0c1d

Emsenhuber, A., Asphaug, E., Cambioni, S., Gabriel, T. S. J., & Schwartz, S. R. 2021, The Planetary Science Journal, 2, 199, doi: 10.3847/PSJ/ac19b1

Fortney, J. J., Marley, M. S., & Barnes, J. W. 2007, The Astrophysical Journal, 659, 1661–1672, doi: 10.1086/512120

Fulton, B. J., Petigura, E. A., Howard, A. W., et al. 2017, The Astronomical Journal, 154, 109, doi: 10.3847/1538-3881/aa80eb

Ginzburg, S., Schlichting, H. E., & Sari, R. 2016, The Astrophysical Journal, 825, 29, doi: 10.3847/0004-637x/825/1/29

—. 2018, Monthly Notices of the Royal Astronomical Society, 476, 759–765, doi: 10.1093/mnras/sty290

Goldreich, P., & Tremaine, S. 1980, The Astrophysical Journal, 241, 425, doi: 10.1086/158356

Grasset, O., Schneider, J., & Sotin, C. 2009, The Astrophysical Journal, 693, 722â733, doi: 10.1088/0004-637x/693/1/722

Guillot, T. 2010, Astronomy and Astrophysics, 520, A27, doi: 10.1051/0004-6361/200913396

Gupta, A., & Schlichting, H. E. 2019, Monthly Notices of the Royal Astronomical Society, 487, 24–33, doi: 10.1093/mnras/stz1230

—. 2020, Monthly Notices of the Royal Astronomical Society, 493, 792â806, doi: 10.1093/mnras/staa315

Hakim, K., Rivoldini, A., Van Hoolst, T., et al. 2018, Icarus, 313, 61–78, doi: 10.1016/j.icarus.2018.05.005

Haldemann, J., Alibert, Y., Mordasini, C., & Benz, W. 2020, Astronomy and Astrophysics, 643, A105, doi: 10.1051/0004-6361/202038367

Han, C., Udalski, A., Jung, Y. K., et al. 2024, Astronomy and Astrophysics, 685, A16, doi: 10.1051/0004-6361/202348791

Hatzes, A. P. 2016, The Radial Velocity Method for the Detection of Exoplanets (Springer International Publishing), 3–86, doi: 10.1007/978-3-319-27458-4_1

Hellard, H., Csizmadia, S., Padovan, S., et al. 2019, The Astrophysical Journal, 878, 119, doi: 10.3847/1538-4357/ab2048

Henry, G. W., Marcy, G. W., Butler, R. P., & Vogt, S. S. 2000, The Astrophysical Journal, 529, L41–L44, doi: 10.1086/312458

Hermes, J. J. 2018, Timing by Stellar Pulsations as an Exoplanet Discovery Method (Springer International Publishing), 787–796, doi: 10.1007/978-3-319-55333-7_6

Hirose, K., Wood, B., & VoÄadlo, L. 2021, Nature Reviews Earth and Environment, 2, 645â658, doi: 10.1038/s43017-021-00203-6

Holland, T. J. B., & Powell, R. 2011, Journal of Metamorphic Geology, 29, 333–383, doi: 10.1111/j.1525-1314.2010.00923.x

Howard, A. W., Marcy, G. W., Bryson, S. T., et al. 2012, The Astrophysical Journal Supplement Series, 201, 15, doi: 10.1088/0067-0049/201/2/15

Howell, S. B., Sobeck, C., Haas, M., et al. 2014, Publications of the Astronomical Society of the Pacific, 126, 398–408, doi: 10.1086/676406

Huang, S.-S. 1959, Publications of the Astronomical Society of the Pacific, 71, 421, doi: 10.1086/127417

Inamdar, N. K., & Schlichting, H. E. 2016, The Astrophysical Journal Letters, 817, L13, doi: 10.3847/2041-8205/817/2/l13

Izidoro, A., Ogihara, M., Raymond, S. N., et al. 2017, Monthly Notices of the Royal Astronomical Society, 470, 1750â1770, doi: 10.1093/mnras/stx1232

Jontof-Hutter, D. 2019, Annual Review of Earth and Planetary Sciences, 47, 141–171, doi: 10.1146/annurev-earth-053018-060352

Jontof-Hutter, D., Ford, E. B., Rowe, J. F., et al. 2016, The Astrophysical Journal, 820, 39, doi: 10.3847/0004-637X/820/1/39

Kasting, J. F., Whitmire, D. P., & Reynolds, R. T. 1993, Icarus, 101, 108â128, doi: 10.1006/icar.1993.1010

Kegerreis, J. A., Eke, V. R., Catling, D. C., et al. 2020, The Astrophysical Journal Letters, 901, L31, doi: 10.3847/2041-8213/abb5fb

Kellermann, C., Becker, A., & Redmer, R. 2018, Astronomy and Astrophysics, 615, A39, doi: 10.1051/0004-6361/201731775

Kley, W., Bitsch, B., & Klahr, H. 2009, Astronomy and Astrophysics, 506, 971–987, doi: 10.1051/0004-6361/200912072

Konacki, M., Torres, G., Sasselov, D. D., & Jha, S. 2003, The Astrophysical Journal, 597, 1076–1091, doi: 10.1086/378561

Kramer, M. 2018, Pulsar Timing as an Exoplanet Discovery Method (Springer International Publishing), 767–786, doi: 10.1007/978-3-319-55333-7_5

Kuchner, M. J., & Seager, S. 2005, Extrasolar Carbon Planets. https://arxiv.org/abs/astro-ph/0504214

Lagrange, A.-M., Bonnefoy, M., Chauvin, G., et al. 2010, Science, 329, 57–59, doi: 10.1126/science.1187187

Lam, K. W. F., Csizmadia, S., Astudillo-Defru, N., et al. 2021, Science, 374, 1271â1275, doi: 10.1126/science.aay3253

Lammer, H., Selsis, F., Ribas, I., et al. 2003, The Astrophysical Journal, 598, L121–L124, doi: 10.1086/380815

Lammer, H., Stökl, A., Erkaev, N. V., et al. 2014, Monthly Notices of the Royal Astronomical Society, 439, 3225, doi: 10.1093/mnras/stu085

Latham, D. W., Mazeh, T., Stefanik, R. P., Mayor, M., & Burki, G. 1989, Nature, 339, 38–40, doi: 10.1038/339038a0

Laughlin, G. 2018, Mass-Radius Relations of Giant Planets: The Radius Anomaly and Interior Models (Springer International Publishing), 1â17, doi: 10.1007/978-3-319-30648-3_1-1

Lee, E. J., & Chiang, E. 2016, The Astrophysical Journal, 817, 90, doi: 10.3847/0004-637x/817/2/90

Lega, E., Morbidelli, A., Bitsch, B., Crida, A., & Szulágyi, J. 2015, Monthly Notices of the Royal Astronomical Society, 452, 1717–1726, doi: 10.1093/mnras/stv1385

Limbach, M. A., Vanderburg, A., Stevenson, K. B., et al. 2022, Monthly Notices of the Royal Astronomical Society, 517, 2622–2638, doi: 10.1093/mnras/stac2823

Lissauer, J. J., Jontof-Hutter, D., Rowe, J. F., et al. 2013, The Astrophysical Journal, 770, 131, doi: 10.1088/0004-637x/770/2/131

Lock, S. J., & Stewart, S. T. 2023, Atmospheric loss in giant impacts depends on pre-impact surface conditions. https://arxiv.org/abs/2309.16399

Lopez, E. D., & Fortney, J. J. 2013, The Astrophysical Journal, 776, 2, doi: 10.1088/0004-637x/776/1/2

—. 2014, The Astrophysical Journal, 792, 1, doi: 10.1088/0004-637X/792/1/1

Lopez, E. D., Fortney, J. J., & Miller, N. 2012, The Astrophysical Journal, 761, 59, doi: 10.1088/0004-637x/761/1/59

Lozovsky, M., Helled, R., Dorn, C., & Venturini, J. 2018, The Astrophysical Journal, 866, 49, doi: 10.3847/1538-4357/aadd09

Lozovsky, M., & Vazan, A. 2024, doi: 10.5194/epsc2024-150

Lupu, R. E., Zahnle, K., Marley, M. S., et al. 2014, The Astrophysical Journal, 784, 27, doi: 10.1088/0004-637x/784/1/27

Luque, R., & Pallé, E. 2022, Science, 377, 1211–1214, doi: 10.1126/science.abl7164

Lustig-Yaeger, J., Meadows, V. S., Tovar Mendoza, G., et al. 2018, The Astronomical Journal, 156, 301, doi: 10.3847/1538-3881/aaed3a

Madhusudhan, N., Lee, K. K. M., & Mousis, O. 2012, The Astrophysical Journal, 759, L40, doi: 10.1088/2041-8205/759/2/l40

Madhusudhan, N., Mousis, O., Johnson, T. V., & Lunine, J. I. 2011, The Astrophysical Journal, 743, 191, doi: 10.1088/0004-637x/743/2/191

Mayor, M., & Queloz, D. 1995, Nature, 378, 355, doi: 10.1038/378355a0

Mennesson, B., Gaudi, S., Seager, S., et al. 2016, in Space Telescopes and Instrumentation 2016: Optical, Infrared, and Millimeter Wave, ed. H. A. MacEwen, G. G. Fazio, M. Lystrup, N. Batalha, N. Siegler, & E. C. Tong, Vol. 9904 (SPIE), 99040L, doi: 10.1117/12.2240457

Mordasini, C., Alibert, Y., & Benz, W. 2009, Astronomy and Astrophysics, 501, 1139â1160, doi: 10.1051/0004-6361/200810301

Mordasini, C., Alibert, Y., Klahr, H., & Benz, W. 2011, EPJ Web of Conferences, 11, 04001, doi: 10.1051/epjconf/20101104001

Mulders, G. D., Pascucci, I., & Apai, D. 2015, The Astrophysical Journal, 814, 130, doi: 10.1088/0004-637x/814/2/130

Mulders, G. D., Pascucci, I., Apai, D., & Ciesla, F. J. 2018, The Astronomical Journal, 156, 24, doi: 10.3847/1538-3881/aac5ea

Nixon, M. C., & Madhusudhan, N. 2021, Monthly Notices of the Royal Astronomical Society, 505, 3414–3432, doi: 10.1093/mnras/stab1500

Otegi, J. F., Bouchy, F., & Helled, R. 2020, Astronomy and Astrophysics, 634, A43, doi: 10.1051/0004-6361/201936482

Owen, J. E., & Campos Estrada, B. 2019, Monthly Notices of the Royal Astronomical Society, 491, 5287–5297, doi: 10.1093/mnras/stz3435

Owen, J. E., & Jackson, A. P. 2012, Monthly Notices of the Royal Astronomical Society, 425, 2931–2947, doi: 10.1111/j.1365-2966.2012.21481.x

Owen, J. E., & Schlichting, H. E. 2023, Monthly Notices of the Royal Astronomical Society, 528, 1615–1629, doi: 10.1093/mnras/stad3972

Owen, J. E., & Wu, Y. 2013, The Astrophysical Journal, 775, 105, doi: 10.1088/0004-637x/775/2/105

—. 2017, The Astrophysical Journal, 847, 29, doi: 10.3847/1538-4357/aa890a

Paardekooper, S.-J., & Mellema, G. 2006, Astronomy and Astrophysics, 459, L17–L20, doi: 10.1051/0004-6361:20066304

Padovan, S., Spohn, T., Baumeister, P., et al. 2018, Astronomy and Astrophysics, 620, A178, doi: 10.1051/0004-6361/201834181

Pepe, F., Ehrenreich, D., & Meyer, M. R. 2014, Nature, 513, 358–366, doi: 10.1038/nature13784

Pepe, F. A., Cristiani, S., Rebolo Lopez, R., et al. 2010, in Ground-based and Airborne Instrumentation for Astronomy III, ed. I. S. McLean, S. K. Ramsay, & H. Takami (SPIE), doi: 10.1117/12.857122

Petigura, E. A., Rogers, J. G., Isaacson, H., et al. 2022, The Astronomical Journal, 163, 179, doi: 10.3847/1538-3881/ac51e3

Plotnykov, M., & Valencia, D. 2020, Monthly Notices of the Royal Astronomical Society, 499, 932–947, doi: 10.1093/mnras/staa2615

Pueyo, L., Zimmerman, N., Bolcar, M., et al. 2017, in UV/Optical/IR Space Telescopes and Instruments: Innovative Technologies and Concepts VIII, ed. H. A. MacEwen & J. B. Breckinridge (SPIE), 15, doi: 10.1117/12.2274654

Rama Murthy, V., & Hall, H. 1970, Physics of the Earth and Planetary Interiors, 2, 276â282, doi: 10.1016/0031-9201(70)90014-2

Rauer, H., Catala, C., Aerts, C., et al. 2014, Experimental Astronomy, 38, 249–330, doi: 10.1007/s10686-014-9383-4

Raymond, S. N., Boulet, T., Izidoro, A., Esteves, L., & Bitsch, B. 2018, Monthly Notices of the Royal Astronomical Society: Letters, 479, L81âL85, doi: 10.1093/mnrasl/sly100

Raymond, S. N., Kokubo, E., Morbidelli, A., Morishima, R., & Walsh, K. J. 2014, Terrestrial Planet Formation at Home and Abroad (University of Arizona Press), doi: 10.2458/azu_uapress_9780816531240-ch026

Raymond, S. N., Quinn, T., & Lunine, J. I. 2005, The Astrophysical Journal, 632, 670, doi: 10.1086/433179

Ricker, G. R., Winn, J. N., Vanderspek, R., et al. 2014, Journal of Astronomical Telescopes, Instruments, and Systems, 1, 014003, doi: 10.1117/1.jatis.1.1.014003

Rogers, J. G., Gupta, A., Owen, J. E., & Schlichting, H. E. 2021, Monthly Notices of the Royal Astronomical Society, 508, 5886–5902, doi: 10.1093/mnras/stab2897

Rogers, J. G., Schlichting, H. E., & Owen, J. E. 2023, The Astrophysical Journal Letters, 947, L19, doi: 10.3847/2041-8213/acc86f

Rogers, L. A. 2015, The Astrophysical Journal, 801, 41, doi: 10.1088/0004-637X/801/1/41

Rogers, L. A., & Seager, S. 2010, The Astrophysical Journal, 712, 974, doi: 10.1088/0004-637X/712/2/974

Santos, N. C., Adibekyan, V., Dorn, C., et al. 2017, Astronomy and Astrophysics, 608, A94, doi: 10.1051/0004-6361/201731359

Saumon, D., Chabrier, G., & van Horn, H. M. 1995, The Astrophysical Journal Supplement Series, 99, 713, doi: 10.1086/192204

Schmitt, J. R., Agol, E., Deck, K. M., et al. 2014, The Astrophysical Journal, 795, 167, doi: 10.1088/0004-637x/795/2/167

Schwarz, R., Bazsó, , Funk, B., & Zechner, R. 2015, Monthly Notices of the Royal Astronomical Society, 453, 2309–2315, doi: 10.1093/mnras/stv1823

Scott, D. 2010, International Statistical Review, 78, 476â477, doi: 10.1111/j.1751-5823.2010.00122_29.x

Seager, S., Kuchner, M., Hier-Majumder, C. A., & Militzer, B. 2007, The Astrophysical Journal, 669, 1279–1297, doi: 10.1086/521346

Shallue, C. J., & Vanderburg, A. 2018, The Astronomical Journal, 155, 94, doi: 10.3847/1538-3881/aa9e09

Smith, A. M. S., Anderson, D. R., Armstrong, D. J., et al. 2014, Astronomy and Astrophysics, 570, A64, doi: 10.1051/0004-6361/201424752

Sohl, F., Wagner, F. W., & Rauer, H. 2012, Proceedings of the International Astronomical Union, 8, 350â355, doi: 10.1017/s1743921313013148

Sotin, C., Grasset, O., & Mocquet, A. 2007, Icarus, 191, 337–351, doi: 10.1016/j.icarus.2007.04.006

Sozzetti, A. 2010, EAS Publications Series, 45, 273–278, doi: 10.1051/eas/1045046

Spaargaren, R., Wang, H., Mojzsis, S., Ballmer, M., & Tackley, P. 2020, doi: 10.5194/egusphere-egu2020-20378

Tateno, S., Hirose, K., Sata, N., & Ohishi, Y. 2009, Earth and Planetary Science Letters, 277, 130–136, doi: 10.1016/j.epsl.2008.10.004

Tey, E., Moldovan, D., Kunimoto, M., et al. 2023, The Astronomical Journal, 165, 95, doi: 10.3847/1538-3881/acad85

Thiabaud, A., Marboeuf, U., Alibert, Y., Leya, I., & Mezger, K. 2015, Astronomy and Astrophysics, 580, A30, doi: 10.1051/0004-6361/201525963

Thomas, S. W., & Madhusudhan, N. 2016, Monthly Notices of the Royal Astronomical Society, 458, 1330â1344, doi: 10.1093/mnras/stw321

Turbet, M., Bolmont, E., Ehrenreich, D., et al. 2020, Astronomy and Astrophysics, 638, A41, doi: 10.1051/0004-6361/201937151

Udalski, A. 2018, Microlensing Surveys for Exoplanet Research (OGLE Survey Perspective) (Springer International Publishing), 1025–1044, doi: 10.1007/978-3-319-55333-7_123

Unger, N., SÃ©gransan, D., Queloz, D., et al. 2021, Astronomy and Astrophysics, 654, A104, doi: 10.1051/0004-6361/202141351

Valencia, D., O'Connell, R. J., & Sasselov, D. 2006, Icarus, 181, 545, doi: https://doi.org/10.1016/j.icarus.2005.11.021

Valencia, D., Sasselov, D. D., & O'Connell, R. J. 2007, The Astrophysical Journal, 665, 1413–1420, doi: 10.1086/519554

Venturini, J., Guilera, O. M., Haldemann, J., Ronco, M. P., & Mordasini, C. 2020, Astronomy and Astrophysics, 643, L1, doi: 10.1051/0004-6361/202039141

Wagner, F., Sohl, F., Hussmann, H., Grott, M., & Rauer, H. 2011, Icarus, 214, 366–376, doi: 10.1016/j.icarus.2011.05.027

Wallace, J., Tremaine, S., & Chambers, J. 2017, The Astronomical Journal, 154, 175, doi: 10.3847/1538-3881/aa8c08

Wang, H. S., Quanz, S. P., Yong, D., et al. 2022, Monthly Notices of the Royal Astronomical Society, doi: 10.1093/mnras/stac1119

Ward, W. R. 1997, Icarus, 126, 261–281, doi: 10.1006/icar.1996.5647

Weidenschilling, S. J., Spaute, D., Davis, D. R., Marzari, F., & Ohtsuki, K. 1997, Icarus, 128, 429, doi: 10.1006/icar.1997.5747

Weiss, L. M., & Marcy, G. W. 2014, The Astrophysical Journal, 783, L6, doi: 10.1088/2041-8205/783/1/l6

Wheatley, P. J., West, R. G., Goad, M. R., et al. 2017, Monthly Notices of the Royal Astronomical Society, 475, 4476–4493, doi: 10.1093/mnras/stx2836

Winn, J. N. 2010. https://arxiv.org/abs/1001.2010

Wright, J. T. 2018, Radial Velocities as an Exoplanet Discovery Method (Springer International Publishing), 619–631, doi: 10.1007/978-3-319-55333-7_4

Zeng, L., & Sasselov, D. 2013, Publications of the Astronomical Society of the Pacific, 125, 227–239, doi: 10.1086/669163

Zeng, L., Sasselov, D. D., & Jacobsen, S. B. 2016, The Astrophysical Journal, 819, 127, doi: 10.3847/0004-637x/819/2/127

Zeng, L., & Seager, S. 2008, Publications of the Astronomical Society of the Pacific, 120, 983â991, doi: 10.1086/591807

Zeng, L., Jacobsen, S. B., Sasselov, D. D., et al. 2019, Proceedings of the National Academy of Sciences, 116, 9723–9728, doi: 10.1073/pnas.1812905116

Zhao, Y., Liu, Z., Ni, D., & Chen, Z. 2024, The Astrophysical Journal Supplement Series, 272, 35, doi: 10.3847/1538-4365/ad3f1c

Étienne Artigau, Bouchy, F., Doyon, R., et al. 2024, NIRPS first light and early science: breaking the 1 m/s RV precision barrier at infrared wavelengths. https://arxiv.org/abs/2406.08304

Appendices

7.1 Mass Fraction

In addition to the core radius fraction,I have also examine the core mass fraction of all studied planets, providing a complementary perspective on their internal composition and density distribution.

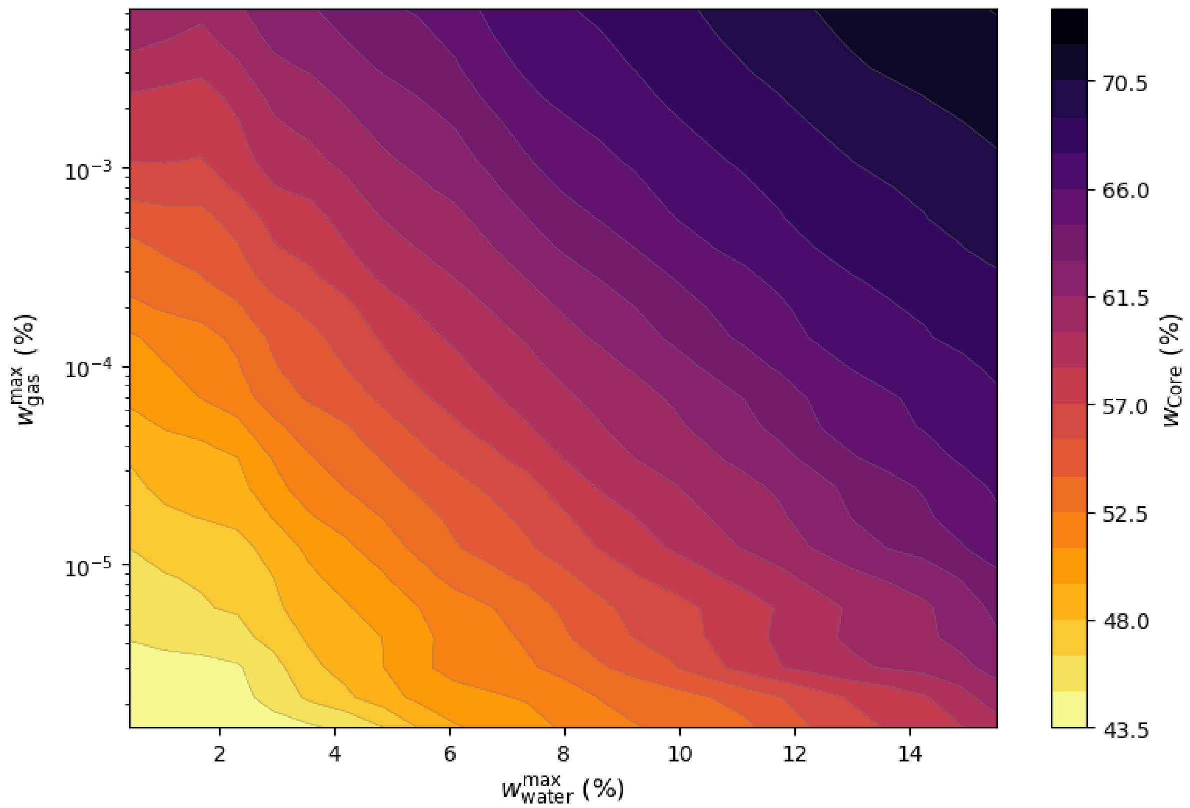

Figure 7.1: Median of the distribution of core radius fractions (w_{core}) as a function of maximum water ($w_{\text{water}}^{\text{max}}$) and gas ($w_{\text{gas}}^{\text{max}}$) content for an Earth-like planet ($1R_{\oplus}$, $1M_{\oplus}$, $T_{\text{eq}} = 255\,\text{K}$), generated using the ExoMDN model. The x-axis represents increasing water content, and the y-axis represents increasing atmospheric content.

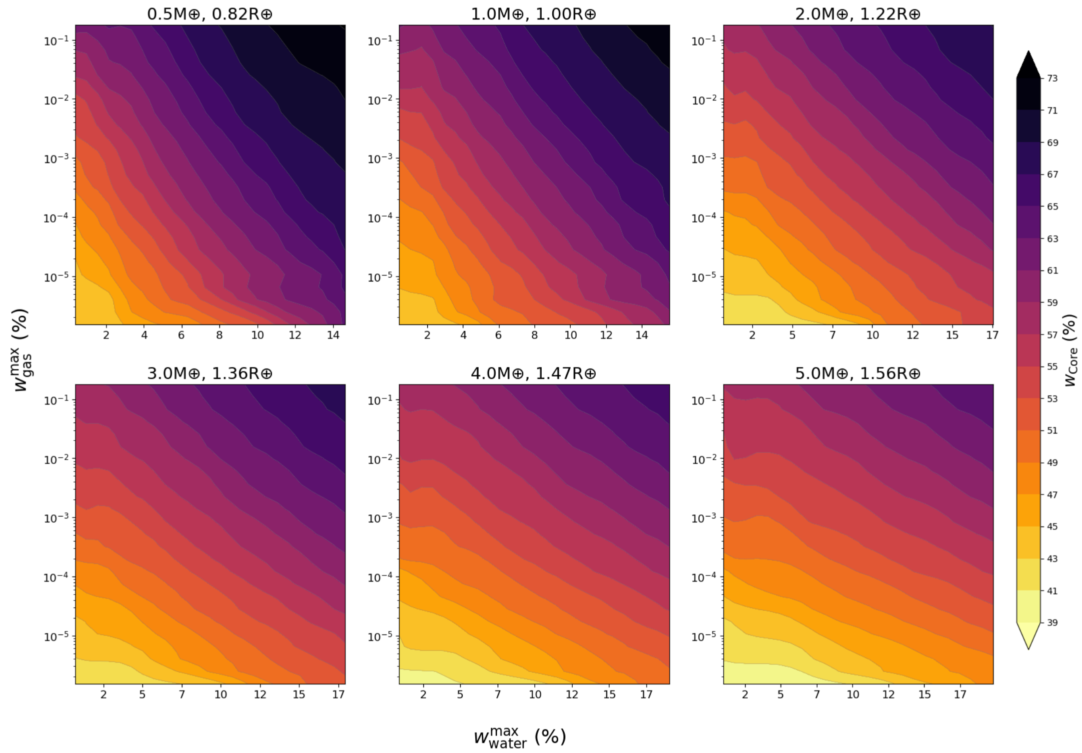

Figure 7.2: The core mass fraction as a function of water and gas fractions plot showing the variation of the core radius fraction (w_{core}) for planets with Earth-like composition with masses ranging from 0.5 to $5M_{\oplus}$. Each panel represents a different planetary mass, with the core mass fraction varying as a function of the maximum allowed water (w_{water}) and gas (w_{gas}) fractions.

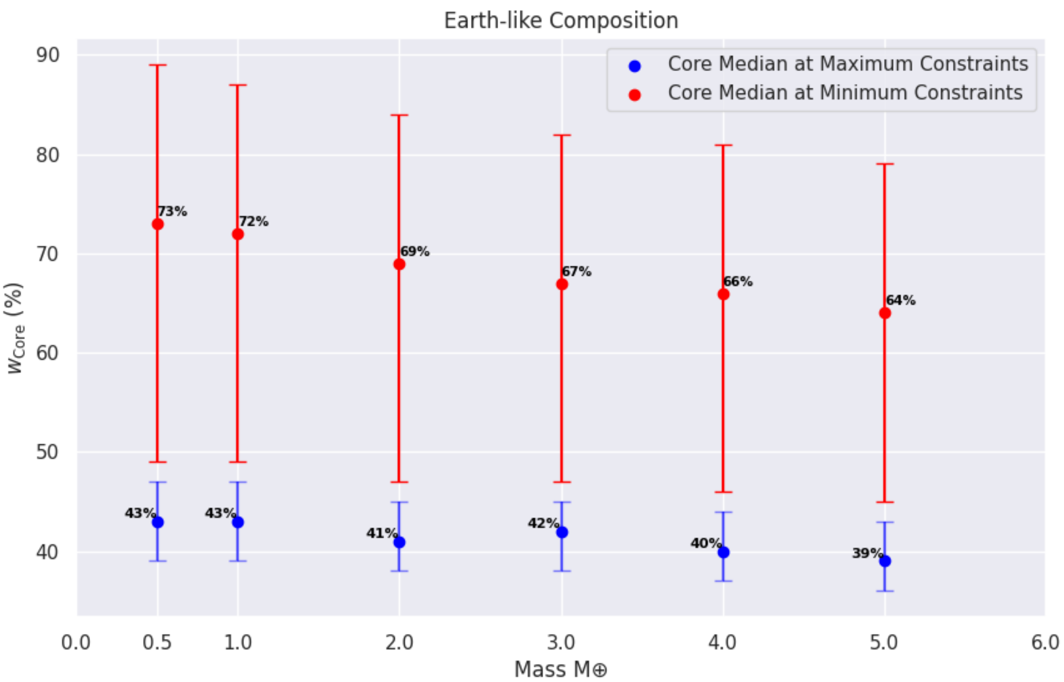

Figure 7.3: The core mass fraction vs. planetary mass plot under maximum and minimum constraints plot for planets with Earth-like composition as a function of planetary mass. The plot shows the median core mass fraction (dots) under two different constraint conditions: minimum constraints (red) and maximum constraints (blue), with error bars indicating the range of variability for each scenario.

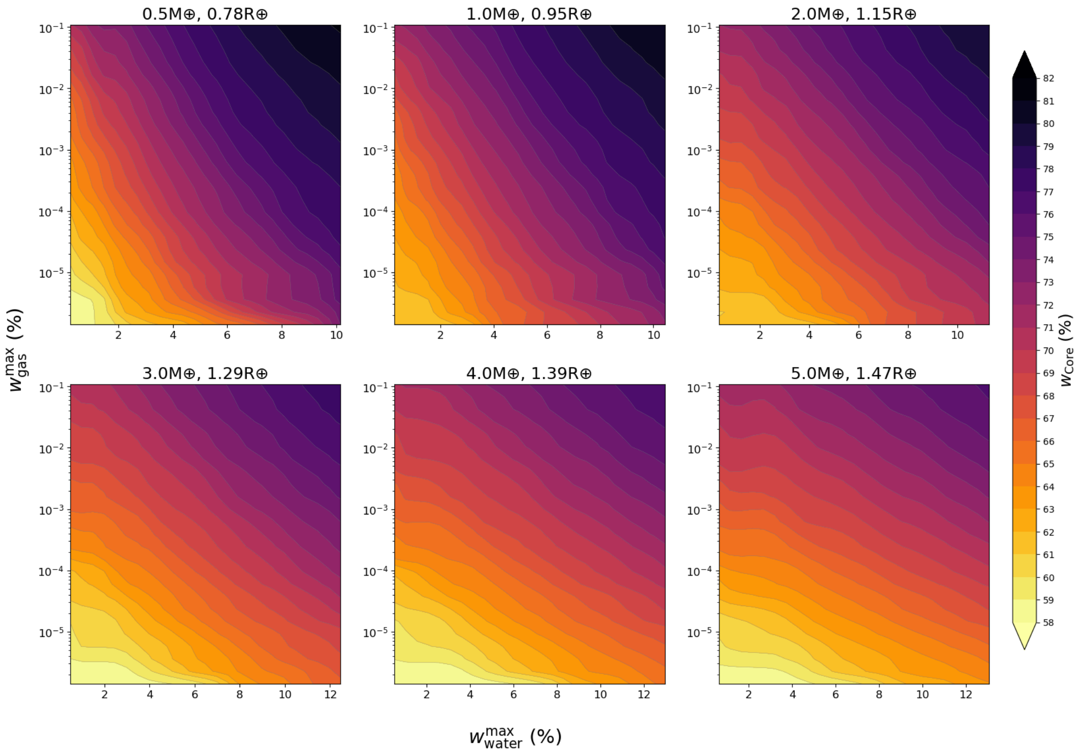

Figure 7.4: The core mass fraction as a function of water and gas fractions plot showing the variation of the core radius fraction ($w_{\rm core}$) for planets with Mercury-like composition with masses ranging from 0.5 to $5M_{\oplus}$. Each panel represents a different planetary mass, with the core mass fraction varying as a function of the maximum allowed water ($w_{\rm water}$) and gas ($w_{\rm gas}$) fractions.

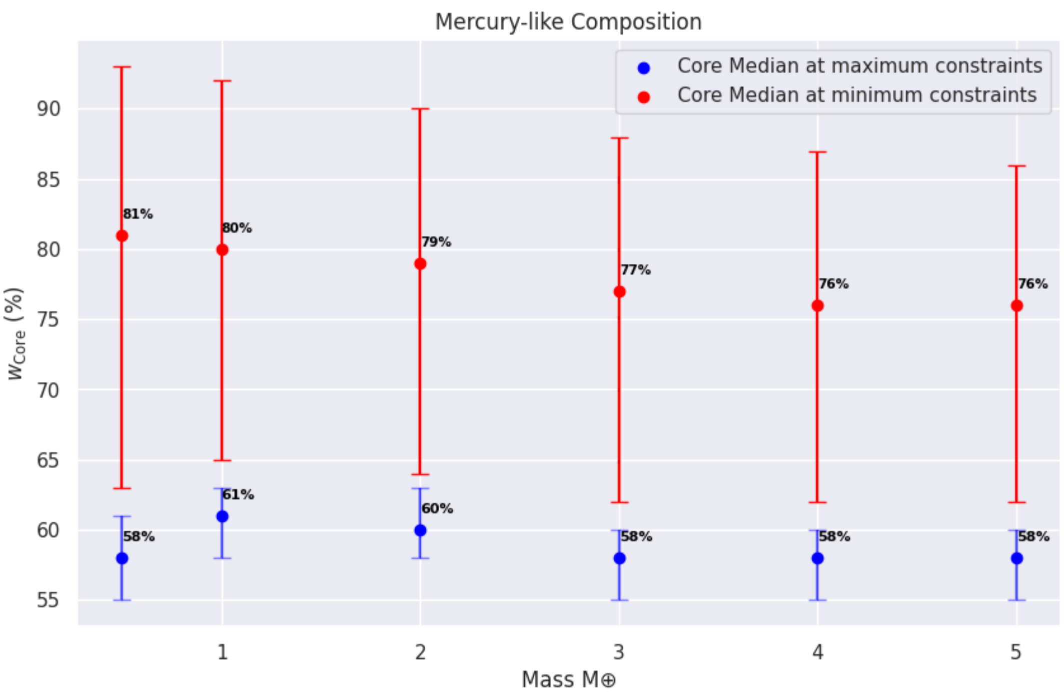

Figure 7.5: The core mass fraction vs. planetary mass plot under maximum and minimum constraints plot for planets with Mercury-like composition as a function of planetary mass. The plot shows the median core mass fraction (dots) under two different constraint conditions: minimum constraints (red) and maximum constraints (blue), with error bars indicating the range of variability for each scenario.

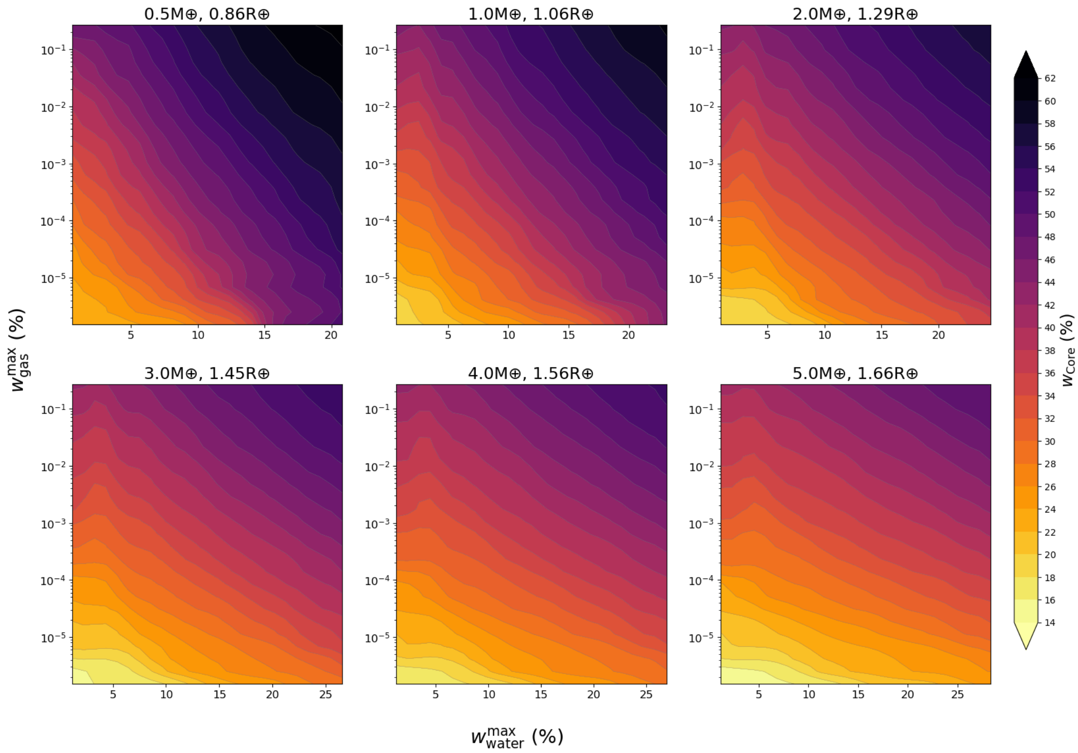

Figure 7.6: The core mass fraction as a function of water and gas fractions plot showing the variation of the core radius fraction (w_{core}) for planets with Moon-like composition with masses ranging from 0.5 to $5M_{\oplus}$. Each panel represents a different planetary mass, with the core mass fraction varying as a function of the maximum allowed water (w_{water}) and gas (w_{gas}) fractions.

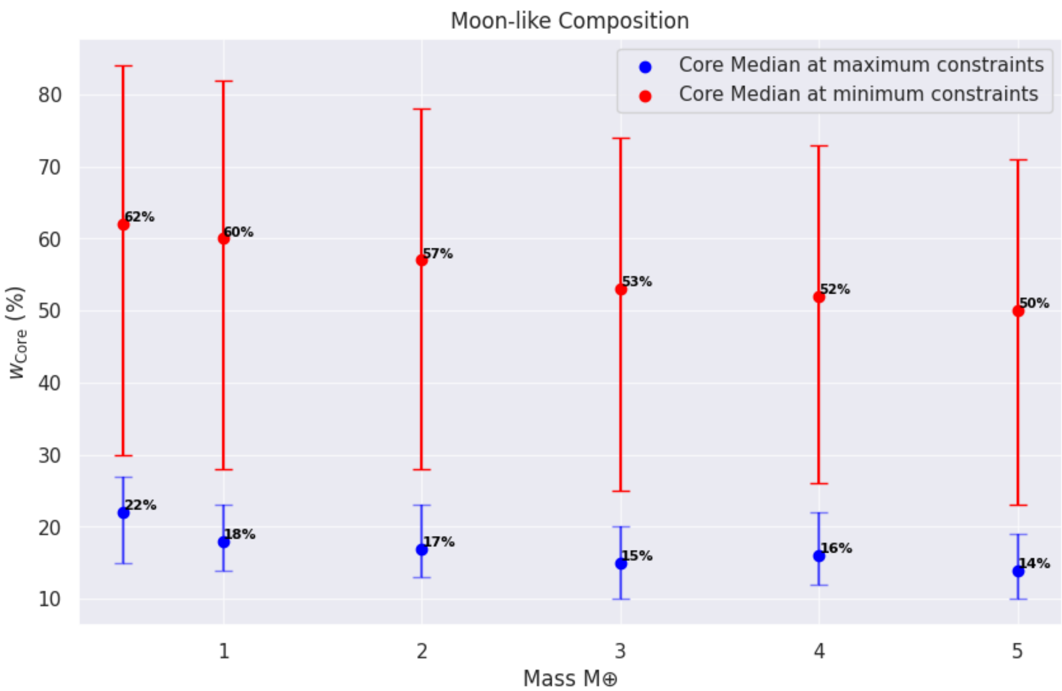

Figure 7.7: The core mass fraction vs. planetary mass plot under maximum and minimum constraints plot for planets with Moon-like composition as a function of planetary mass. The plot shows the median core mass fraction (dots) under two different constraint conditions: minimum constraints (red) and maximum constraints (blue), with error bars indicating the range of variability for each scenario.